№4, 2023

ISSN 2706-977X

70

SAGINOV TECHNICAL UNIVERSITY

# MATERIAL AND MECHANICAL ENGINEERING TECHNOLOGY

Material and Mechanical Engineering Technology | MMET

**Editorial board of the journal**

**Content**

**DOI 10.52209/2706-977X_2023_4_3** **IRSTI 53.49.19** **UDC 681.2.088**

# Estimation of Temperature Effects on Uncertainties of Dimensional Measurements in Industrial Computed Tomography by Finite Element Modeling

**Drégelyi-Kiss Á.*, Anh Dao Duy, Farkas G., Gonda V.**
Óbuda University, Budapest, Hungary
*corresponding author

**Abstract.** Using industrial computed tomography (CT) in measuring dimensional parameters (such as diameter, distance) of manufactured parts becomes more and more popular due to its advantages such as being a non-destructive method and possibility to complete complex shape measurements rapidly. However, the accuracy and precision of the measured values are required to be validated by quality control. The complicated structure of multi-step processing contribute to measurement errors and uncertainties through various factors. Among them, temperature change during the operation of CT machine possesses a high potential influence. Two test geometries created in Catia V5 were modelled in Marc Mentat Finite Element software considering different materials (PMMA, Al, AlMgSi1) to study the deformation behavior against the change of temperature during the CT measurement process. The results of simulations provided an appropriate point of view about the effect of the temperature parameter to the measurement accuracy and uncertainties.

**Keywords:** dimensional metrology, CT measurements, measurement error, measurement uncertainty, finite element modeling, temperature effects.

## Introduction

In modern industry, dimensional metrology is essential for quality control. Until now, optical and tactile systems have been popular because of their accuracy and the certificated uncertainties. However, for the purpose of evaluation the internal structure of a part or an assembly, these systems face real challenges.

In recent years, CT dimensional measurements have emerged as a solution to the difficulties of controlling the overall structure of the product [1]. Known as a non-destructive method, CT can map 2D, or 3D images of objects, which are directly processed by assistant software (such as VGS studio [2] to implement dimensional metrology's requirements, in a short time.

Notwithstanding, because of the complexity of CT systems and the measurement strategy, data traceability becomes extraordinarily difficult. Figure 1 introduces comprehensively factors influencing the performance of CT system in dimensional metrology [3,4].

Because there are variety of sources can contribute to measurement errors and uncertainties, research about them becomes essential and popular. About the impact of X-ray source, research about the effect of focal spot size, focus drift and tube power (including voltage, current) were implemented [5,6,7]. The influence of material, temperature and surface roughness of specimen were also investigated by several authors [8,9,10,11,12,13]. On the other hand, the detector contributes to measurement errors through main parameters such as detective quantum efficiency and image lag [5,14]. The step of image processing possibly affects to the accuracy of metrology measurement [15,17].

In 2015, an experiment implemented by H. Villarraga-Gomez [11,12], specimens with identical geometry but different material quality were measured by CT method, and studied the effect of external parameter influences for the accuracy of measurements. The temperature change at position of workpiece were also recorded. Features were measured at different stages of CT processing to determine the behavior of measurement uncertainties under the effect of temperature.

In this paper, two specimens with different structures were modelled in simulated to evaluate how the distribution of measurement errors caused by changing of temperature will be. Furthermore, the results of simulations were compared with the work of H. Villarraga-Gomez to compare the compensation of temperature change used in [11,12].

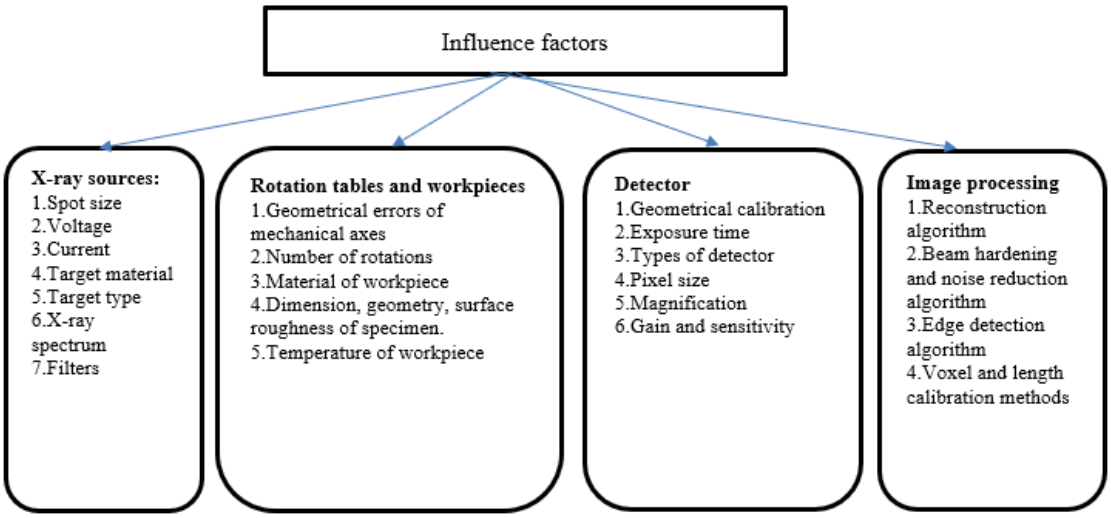


**Fig. 1.** – Influencing factors on dimensional metrology by CT

## 1. Materials and Methods

### 1.1 Theoretical background

Followed by the Guide to the Expression of Uncertainty in Measurement (GUM) (clause 3.2.4) [19] and with the assumption that the same application from ISO 15530 for tactile CMMs [20] was used for X-ray CT in measurement uncertainties estimation, the correct measurement result by CT system $X_{corr}$ of n independent observations which has arithmetic mean $\bar{X}_{CT}$ can be calculated as follows:

$$X_{corr} = \bar{X}_{CT} - b \pm U_{CT} \tag{1}$$

where $b$ is the bias of systematic errors calculated by the $\bar{X}_{CT}$ minus the true value (reference value) measured by a more accurate system than CT (CMMs). $U_{CT}$ is equal to $k \cdot u_{CT}$ with k = 2 for confidence interval of 95% and $u_{CT}$ is a quadratic sum of several basic contributions [18,20]:

$$u_{ct} \approx \sqrt{{u_{ref}}^2 + {u_p}^2 + {u_w}^2 + {u_b}^2} \tag{2}$$

where $u_{ref}$ is the standard uncertainties of reference value or in certificated calibration procedure for the specimen. It is normally assumed that this value is negligible in comparison with other elements in (2). Parameter $u_p$is the uncertainty of repeatability and $u_w$ is the variation as a consequence of expansion due to temperature change or surface roughness. As a component of $u_w$, the uncertainties in the temperature change is considered as the largest influence. It was calculated by the Eq. (3) [11,12]:

$$u_T \approx \beta L|\Delta T|/\sqrt{3} \tag{3}$$

where $\beta$ is the expansion coefficient, $L$ is the length of the measurand (in meter) and $\Delta T$ is the change of temperature projected to the reference temperature (20°C). Constant of $\sqrt{3}$ illustrates for the assumption of the rectangular error distribution for temperature. Finally, $u_b$ is the standard uncertainty caused by systematic errors of the calibration measurement procedure includes two main contributors: deviation between CT measurement and reference values and the uncertainty due to thermal expansion for the calibrated workpiece. Generally, if systematic errors are compensated, Eq. (2) will be used. However, in case of being not fully compensated, the formula was proposed in ISO/TS 15530-3:2009 [20] will be used:

$$u_{ct} \approx \sqrt{{u_{ref}}^2 + {u_p}^2 + {u_w}^2 + b^2} \tag{4}$$

### 1.2 Materials and models

Two test geometries were defined for the analysis. The geometry of the first sample for this study was a rectangular block (referred hereafter as the 'hole block') with outer dimensions of 20 mm × 40 mm × 60 mm with a 10 mm diameter hole passing through the center of the longest axis (Figure 2a). The used materials for this geometry were poly(methyl methacrylate) (PMMA) and aluminum.

The second geometry was made of aluminum alloy (AlMgSi1). It has the shape of a cube with the size of 90 mm × 90 mm × 90 mm. In this block, 14 holes were defined with a distributed layout as in the Figure 1b. The physical parameters of materials are listed in Table 1.

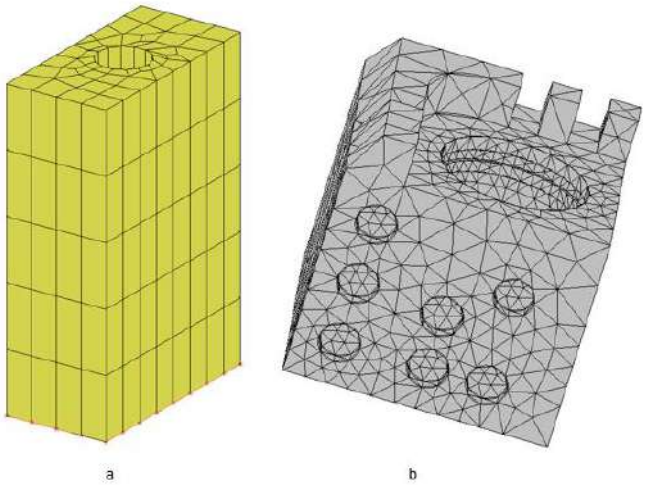


**Fig. 2.** – Test geometries with finite element mesh the first geometry (a), the second geometry (b).

**Table 1.** The parameters of materials

| ***Type of parameters*** | ***PMMA*** | ***Aluminum*** | ***AlMgSi1*** |
|---|---|---|---|
| Mass density | $1.18\times10^{6}\ kg/m^{3}$ | $2.7\times10^{6} kg/m^{3}$ | $2.7\times10^{6}\ kg/m^{3}$ |
| Thermal conductivity | $0.21\ Wm^{-1}K^{-1}$ | $237\ Wm^{-1}K^{-1}$ | $195\ Wm^{-1}K^{-1}$ |
| Specific heat | $1466\ Jkg^{-1}K^{-1}$ | $898.7\ Jkg^{-1}K^{-1}$ | $900\ Jkg^{-1}K^{-1}$ |
| Young modulus | 2450 MPa | 70 GPa | 70 GPa |
| Poisson ratio | 0.375 | 0.33 | 0.33 |
| Thermal expansion | $126\ \mu m\ m^{-1}{}^{\circ}C^{-1}$ | $23.4\ \mu m\ m^{-1}{}^{\circ}C^{-1}$ | $23.4\ \mu m\ m^{-1}{}^{\circ}C^{-1}$ |

## 2. Method

Finite element method (FEM) was employed in Marc Mentat, which is a popular method for solving problems of engineering and mathematical models. In FEM, geometry is divided into a large system of small, simpler parts called elements, which is implemented by the construction of a mesh of object. The simple equations modelling the finite one will be assembled into a larger system of equations modelling entire problem. Marc Mentat is a popular software could use FEM to handle with complicated issues [21]

There are several common parameters among simulations. Constraints for displacements are applied to 4 points at corners of the bottom of workpieces. The distribution of temperature is assumed to be uniform over the whole solid part. The varied parameter in this simulation was the temperature, temperature data were used as in [11,12]. There were 5 regions:

- Region 1: the warm up phase (X-ray was turned on) lasted 1-1.5 hour and temperature increased up to 22°C
- Region 2: the X-ray was turned off in 4.5-5h. Temperature decreases to 21.4°C at the end of phase.
- Region 3: X-ray was turned on to make measurement. The temperature raised to 22.15°C at the end of phase 3. This stage lasted 3 hours.
- Region 4: CT maintain active whole the region in 8 hours. The temperature reached the highest value during operation (22.45°C)
- Region 5: Power tube was turned off. The temperature went down to 21.9°C.

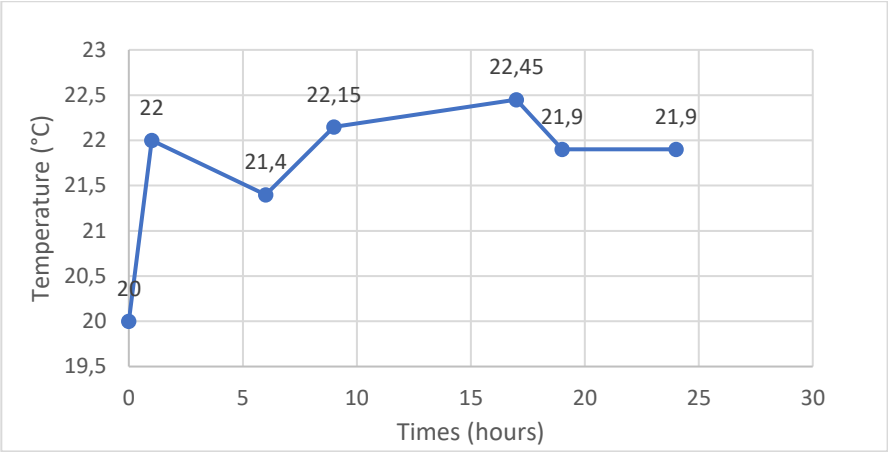


**Fig. 2.** – Graph of temperature change used in simulation

Fig. 3 illustrates the changes in temperature for each region. The simulation was divided in to 2 phases:

Phase 1: Using the information about temperature in Fig. 3 to simulate the behavior of two model under the effect of temperature change. From this phase, the distribution of displacement will be revealed. The maximum value of displacement will also be recorded.

Phase 2: At the end of region 5 the temperature decreased to 21.9°C which is the average temperature used in [11,12] for calculating the compensated value. The value in simulation at this temperature will be recorded and made comparison to evaluate if we can simply use Eq. (5) to calculate the corrected value:

$$\Delta l \approx \beta l \Delta T \tag{5}$$

The time for scanning by CT usually lasts several hours that is extremely long for simulation. Therefore, unit of hour was converted to second with respect ratio (1 hour was converted to 1 second in simulation)

**Simulation results**

Four types of results were extracted: displacement field in x,y,z-direction and the total displacement field displayed by vectors.

**Table 2.** Node has max value and max value of first model made of PMMA

| | *Node has max value of displacement* | *Max value of displacement [μm]* |
|---|---|---|
| *In x direction* | 1, 2 | -6.29,6.28 |
| *In y direction* | 3, 4 | 3.751, -3.712 |
| *In z direction* | 5 | 22.44 |
| *Total displacement* | 5 | 23.47 |

**Table 3.** Node has max value and max value of first model made of Aluminum

| | *Node has max value of displacement* | *Max value of displacement [μm]* |
|---|---|---|
| *In x direction* | 1,2 | -1.166, 1.165 |
| *In y direction* | 3,4 | 0.683, 0.677 |
| *In z direction* | 5 | 4.127 |
| *Total displacement* | 5 | 4.322 |

**Table 4.** Node has max value and max value of second model made of AlMgSi1

| | *Node has max value of displacement* | *Max value of displacement [μm]* |
|---|---|---|
| *In x direction* | 7,8 | 3.052, -2.785 |
| *In y direction* | 9,10 | 2.888, -2.591 |
| *In z direction* | 11 | 7.582 |
| *Total displacement* | 12 | 8.173 |

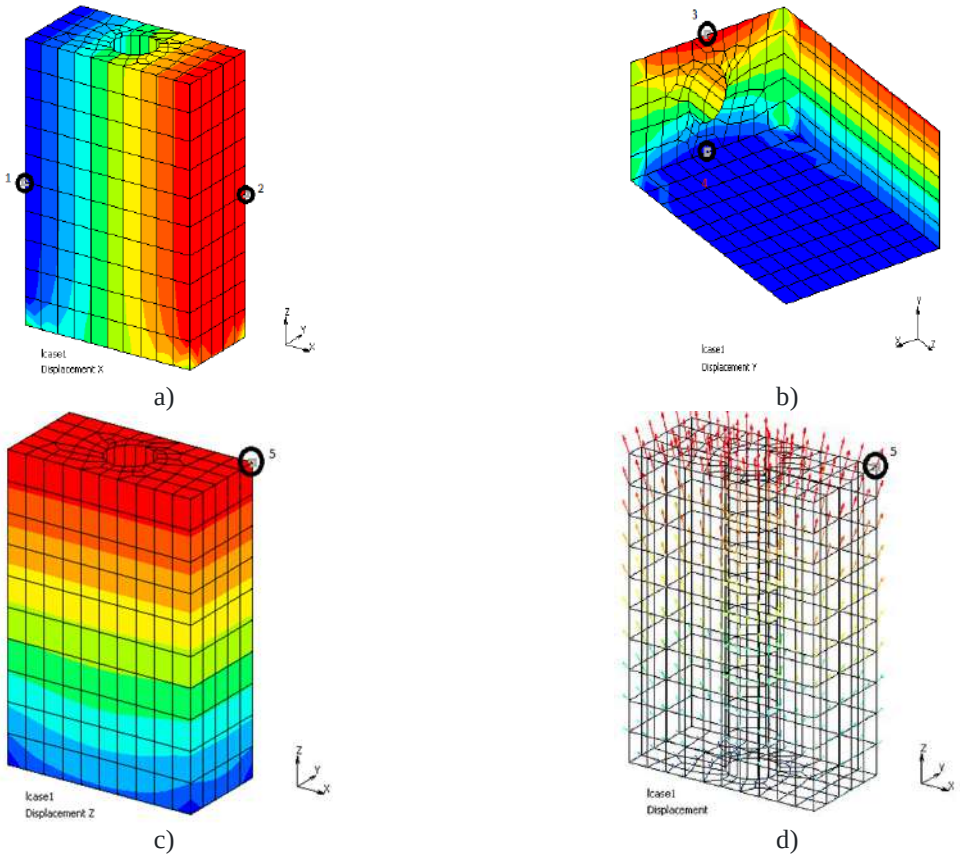


**Fig. 3.** – The displacement of the first model made of PMMA under simulation. a) x-direction, b) y-direction displacement, c) z-direction displacement, d) total displacement.

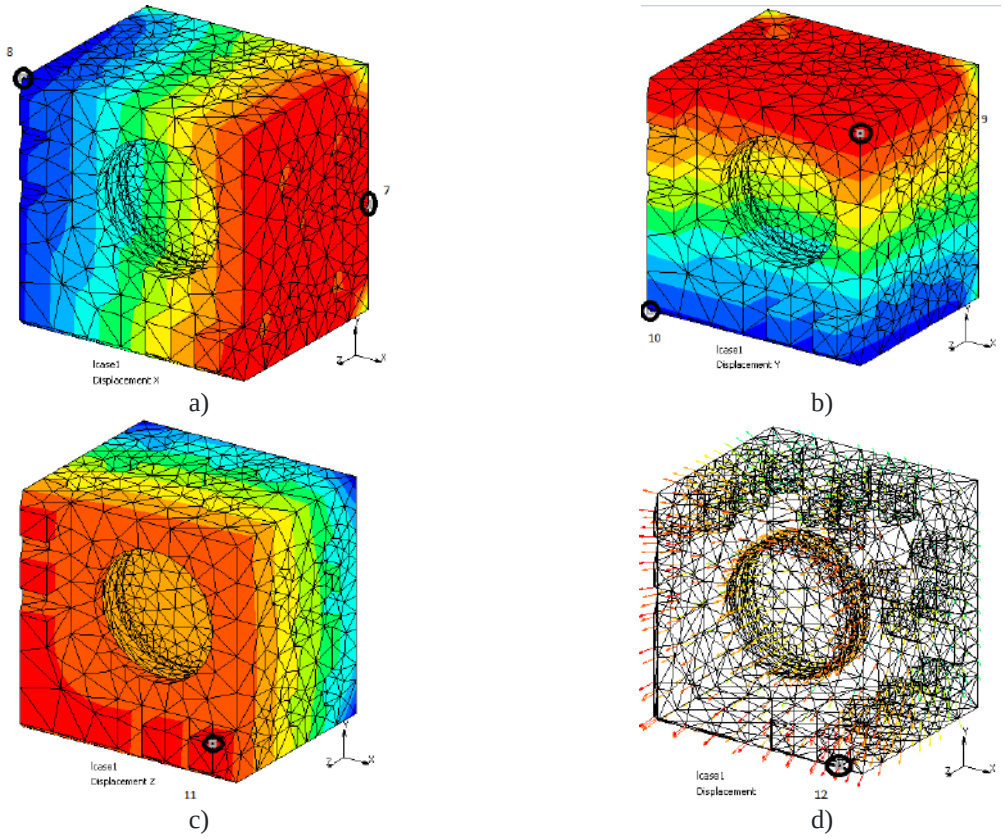


**Fig. 4.** – The displacement of the second model made of AlMgSi1 under simulation: a) x-direction, b) y-direction displacement, c) z-direction displacement, d) total displacement

Fig. 6 shows the spectrum of displacements.

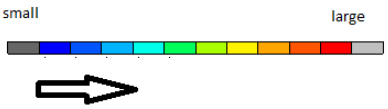


**Fig. 5.** – Spectrum of displacements

As the coordinate axes located at the center and bottom of the workpiece on XY plane, the displacement in X and Y direction had both sign while Z-direction ad total displacement only had positives sign. Table 2-4 recorded the largest value of 4 types of displacements at the highest temperature (22.45°C) and Fig. 5 and Fig. 6 illustrated the position having those values.

Several conclusions could be drawn for the first phase of simulation:

- In x and y direction, the displacement is the lowest at the middle of the model and larger when reach edges;
- In z direction, the displacement is the lowest at the bottom and is the highest at the top of the model;
- The displacement in z direction dominated the maximum value of total displacement;
- The node has the maximum displacement in total will be at the max value point of z displacement or near that PMMA has larger expansion coefficient so that the displacement is significant bigger than the two rest cases (Aluminum and AlMgSi1 have similar expansion coefficients).

In [11,12], the first model's dimensional parameters were measured including length and width of 5 rectangles and the height. To compensate for the change of temperature, Eq. (5) was used and the average temperature for whole process was assumed to be 21.9°C with PMMA and 22.3°C with Al. With the simulation, value of displacements was recorded at the same temperature. The Eq. (6) illustrates how to calculated the distance between two points A $(x_A, y_A, z_A)$ and B $(x_B, y_B, z_B)$ which have the displacement respectively in direction x, y and z $\boldsymbol{\Delta}$A $(\Delta x_A, \Delta y_A, \Delta z_A)$ and $\boldsymbol{\Delta}$B $(\Delta x_B, \Delta y_B, \Delta z_B)$:

$$ND(new\ distance) = \sqrt{(x_A + \Delta x_A - x_B - \Delta x_B)^2 + (y_A + \Delta y_A - y_B - \Delta y_B)^2 + (z_A + \Delta z_A - z_B - \Delta z_B)^2} \quad (6)$$

$$OD(original\ distance) = \sqrt{(x_A - x_B)^2 + (y_A - y_B)^2 + (z_A - z_B)^2} \quad (7)$$

$$ME(measurement\ error) = ND - OD \quad (8)$$

Applying the above equation, Table 5 compare the corrected value used in [11,12] and the corrected value calculated by simulation.

**Table 5.** Comparison between corrected values between using Eq.(3) and simulations

| *Dimensional parameters* | *Corrected values by equations [μm]* | | *Corrected values by simulations [μm]* | |
|---|---|---|---|---|
| | PMMA | Al | PMMA | Al |
| Width | 5 | 1 | 5.208 | 1.360 |
| Length | 10 | 2 | 9.748 | 2.331 |
| Heigh | 14 | 3 | 15.66 | 4.127 |

The deviations between corrected values are normally smaller than 1 μm which can be considered neglectable. On the other hand, the results of Eq. (5) are usually smaller than from the simulations.

**Conclusions**

With installed cooling systems, computed tomography is expected to maintain ideal temperature during the process of measurement. However, the expectation cannot be fulfilled, which was proved in [11,12] with the change of temperature. Consequently, measurement errors caused by thermal expansion are inevitable. The simulation of temperature change's effect was implemented on 2 models with different materials where thermal expansion coefficients are distinctive to reveal the possible errors.

With Marc Mentat and FEM method, the distribution of displacement in whole body of specimens were illustrated. It was also proved that maximum displacements for aluminum material is under 5 μm and for PMMA is under 20 μm for both models. In previous work, corrected values were calculated by Eq. (5) to compensate the change in temperature, which was compared with the value from the simulation. With the deviation under 1 μm, it can be concluded that using Eq. (5) to calculate compensated value if temperature during CT process cannot be maintained at 20 °C is applicable to simplify the work of determining the results of measurement.

**References**

[1] Villarraga-Gómez, H., Morse, E. P., Hocken, R. J., & Smith, S. T. (2014). Dimensional metrology of internal features with X-ray computed tomography // Proc. of 29th ASPE Annual meeting, 2014, P. 684-689.

[2] Reinhart, C. (2008, October). Industrial computer tomography–a universal inspection tool. In 17th world conference on nondestructive testing, P. 25-28.

[3] Kruth, J. P., Bartscher, M., Carmignato, S., Schmitt, R., De Chiffre, L., & Weckenmann, A. (2011). Computed tomography for dimensional metrology. CIRP annals, 60(2), P. 821-842.

[4] Welkenhuyzen, F., Kiekens, K., Pierlet, M., Dewulf, W., Bleys, P., Kruth, J. P., & Voet, A. (2009). Industrial computer tomography for dimensional metrology: Overview of influence factors and improvement strategies. In Proceedings of the 4th international conference on optical measurement techniques for structures and systems: Optimess 2009, P. 401-410.

[5] Hiller, J., Maisl, M., & Reindl, L. M. (2012). Physical characterization and performance evaluation of an x-ray micro-computed tomography system for dimensional metrology applications. Measurement Science and Technology, 23(8), 085404.

[6] Drégelyi-Kiss, Á. (2019, June). Towards Traceable Dimensional Measurements by Micro Computed Tomography. In International Conference on Measurement and Quality Control-Cyber Physical Issue (pp. 247-254). Springer, Cham

[7] Dao, A., & Drégelyi-Kiss, Á. (2020). Determination of GD&T Features Varying the Setting Parameters of X-Ray Computed Tomography by Response Surface Method. In Materials Science Forum (Vol. 994, pp. 280-287). Trans Tech Publications Ltd.

[8] Aloisi, V., & Carmignato, S. (2016). Influence of surface roughness on X-ray computed tomography dimensional measurements of additive manufactured parts. Case studies in nondestructive testing and evaluation, 6, 104-110

[9] Villarraga, H., Morse, E., Hocken, R., & Smith, S. (2014). A study on material influences in dimensional computed tomography. In Proceedings–ASPE 2014 annual meeting (pp. 67-72).

[10] Su, S., Dai, N., Cheng, X., Zhou, X., Wang, L., & Villarraga-Gómez, H. (2019). A Study on Factors Influencing the Accuracy Evaluation of Dimensional X-Ray Computed Tomography with Multi-sphere Standards. International Journal of Precision Engineering and Manufacturing, 1-13.

[11] Villarraga-Gómez, H., Thousand, J. D., Morse, E. P., & Smith, S. T. (2015). CT measurements and their estimated uncertainty: The significance of temperature and bias determination. In ASPE Mets & Props, 60, J. Phys.: Conf. Ser.

[12] Villarraga-Gómez, H., Thousand, J. D., & Smith, S. T. (2020). Empirical approaches to uncertainty analysis of X-ray computed tomography measurements: A review with examples. Precision Engineering, 64, 249-268.

[13] Bartscher, M., Illemann, J., & Neuschaefer-Rube, U. (2016). ISO test survey on material influence in dimensional computed tomography. Case studies in nondestructive testing and evaluation, 6, 79-92.

[14] Wenig, P., & Kasperl, S. (2006, September). Examination of the measurement uncertainty on dimensional measurements by X-ray computed tomography. In Proceedings of 9th European Conference on Non-Destructive Testing (ECNDT), Berlin, Germany.

[15] Drégelyi-Kiss, Á., & Durakbasa, N. M. (2018, August). Measurement error on the reconstruction step in case of industrial computed tomograph. In The International Symposium for Production Research (pp. 309-323). Springer, Cham.

[16] Bartscher, M., Sato, O., Härtig, F., & Neuschaefer-Rube, U. (2014). Current state of standardization in the field of dimensional computed tomography. Measurement Science and Technology, 25(6), 064013.

[17] Hiller, J., Fuchs, T. O., Kasperl, S., & Reindl, L. M. (2011). Influence of the quality of X-ray computed tomography image on coordinate measurements. Principles, measurements and simulations. TM. Technisches Messen, 78(7-8), 334-347.

[18] Villarraga-Gómez, H., Lee, C., & Smith, S. T. (2018). Dimensional metrology with X-ray CT: A comparison with CMM measurements on internal features and compliant structures. Precision Engineering, 51, 291-307.

[19] Therefore, S. T. C., & AS, M. (1993). Guide to the Expression of Uncertainty in Measurement.

[20] ISO 15530-3 (2011), Geometrical product specifications (GPS)-Coordinate measuring machines (CMM): Technique for determining the uncertainty of measurement -Part 3: Use of calibrated workpieces or measure standards, Geneva (Switzerland): ISO copyright office.

**Information of the authors**

**Ágota Drégelyi-Kiss**, associate professor, Óbuda University, Budapest, Hungary
e-mail: dregelyi.agota@bgk.uni-obuda.hu

**Anh Dao Duy**, PhD student, Óbuda University, Budapest, Hungary
e-mail: duyanhbmehust@gmail.com

**Farkas Gabriella,** PhD, associate professor, Óbuda University, Budapest, Hungary
e-mail: farkas.gabriella@bgk.uni-obuda.hu

**Viktor Gonda**, associate professor, Óbuda University, Budapest, Hungary, corresponding author
e-mail: gonda.viktor@bgk.uni-obuda.hu

**DOI 10.52209/2706-977X_2023_4_10 IRSTI 55.19.13 UDC 621.941.1**

# Evaluation of the Structural Strength of a Prefabricated Milling Cutter with Replaceable inserts During Machining

**Nurzhanova O.*, Zharkevich O., Berg A., Zhukova A., Mussayev M, Buzauova T., Abdugaliyeva G., Shakhatova A.**
Abylkas Saginov Karaganda Technical University, Karaganda, Kazakhstan
*corresponding author

**Abstract:** Simulation modeling of the stress state of a prefabricated milling cutter with replaceable inserts during machining was carried out in the ABAQUS 2020 program using the finite element method. It has been established that the structural strength of a cutting tool depends on the geometry, material and cutting conditions. Based on the simulation, stress concentrators in a milling cutter with replaceable inserts were identified. The safety factor of the structure has also been determined, which meets the standard requirement. It has been established that a prefabricated milling cutter with replaceable plates during machining under extreme conditions ensures its performance with a margin of 20%. Thus, a prefabricated cutter with replaceable inserts is applicable for machining newly created and restored surfaces after hardfacing.

**Key words:** FEM-analysis, stress, safety factor, fatigue strength.

**Inrtroduction.**

The trends in the modern cutting tool market are such that in order to maintain competitiveness, cutting tool manufacturers are forced to constantly look for new solutions to ensure the efficiency of machining. Experiments are constantly being carried out with the shape of the cutting edge in order to ensure cutting at higher speeds and at the same time obtain better quality milled surfaces [1].

Currently, cutting tools equipped with carbide replaceable polyhedral inserts in the shape of polyhedra (triangles, squares, rhombuses, etc.), each side of which is a cutting edge, are increasingly used. The plates are attached to the tool bodies using special devices that allow them to be rotated around their axes, introducing a new cutting edge into the working position instead of a dull one [2].

It is also important to develop tools for mechanical processing of surfaces after restoration by surfacing. The deposited layer is quite hard and the tool experiences a lot of wear during machining. For this purpose, you can also use a cutting tool with replaceable polyhedral inserts.

When creating a new cutting tool, the strength of the structure is assessed using the finite element method.

The finite element method is the main method of modern computational mechanics, which underlies the vast majority of modern software systems designed to perform calculations of engineering structures on a computer [3].

The finite element method makes it possible to almost completely automate the calculation of mechanical systems, although, as a rule, it requires a significantly larger number of computational operations compared to classical methods of mechanics of a deformable solid [4].

The finite element method allows you to construct a convenient scheme for forming a system of algebraic equations with respect to the nodal values of the desired function. Approximate approximation of the solution using simple polynomial functions and all necessary operations are performed on a separate standard element [5]. Then the elements are combined, which leads to the required system of algebraic equations. This algorithm for transition from a single element to their complete set is especially convenient for geometrically and physically complex systems. Each individual algebraic equation obtained on the basis of the finite element method contains an insignificant part of the nodal unknowns from their total number. In other words, many coefficients in the equations of an algebraic system are equal to zero, which greatly facilitates its solution [6].

For strength calculations, the finite element method is often used in various software.

One such program is ABAQUS, a universal general-purpose system designed both for multi-purpose engineering multidisciplinary analysis and for research and educational purposes in a wide variety of fields. This package can be used at all stages of the design and creation of modern products [7].

ABAQUS meets the ISO 9001 quality standard and the quality standard established by the American Nuclear Review Board for quality assurance of nuclear power plant design (ANSI/ASME NQA-1, 1983). Also, the results obtained using the ABAQUS software package show the validity of the results, reaching 98% [8].

The task of choosing a rational design of cutting tools is complex and time-consuming, requiring the synthesis and evaluation of a large number of combinations of structural options for assembly structural elements, the values of their parameters and the materials from which they are made. The rationality of the form and the correctness of the chosen material determine the strength of the cutting tool design.

Therefore, the purpose of this article is to develop a methodology for assessing the strength of a new design of a prefabricated cutter with replaceable inserts for processing restored spline surfaces using surfacing methods.

## 1. Research methodology

Modeling of the stress state of a prefabricated cutter with replaceable inserts was carried out in the ABAQUS 2020 program. When modeling the stress state of a prefabricated cutter with replaceable inserts, it is important to correctly generate the correct finite element mesh (FEM). The meshing process used three-dimensional second-order HEXA FEMs (hex elements) to accurately represent the distribution of internal stresses in the samples under the influence of external forces [9]. Figure 1 shows the mesh applied to an assembly cutter with replaceable inserts. The prefabricated cutter was divided into 67,872 nodes and 62,000 elements.

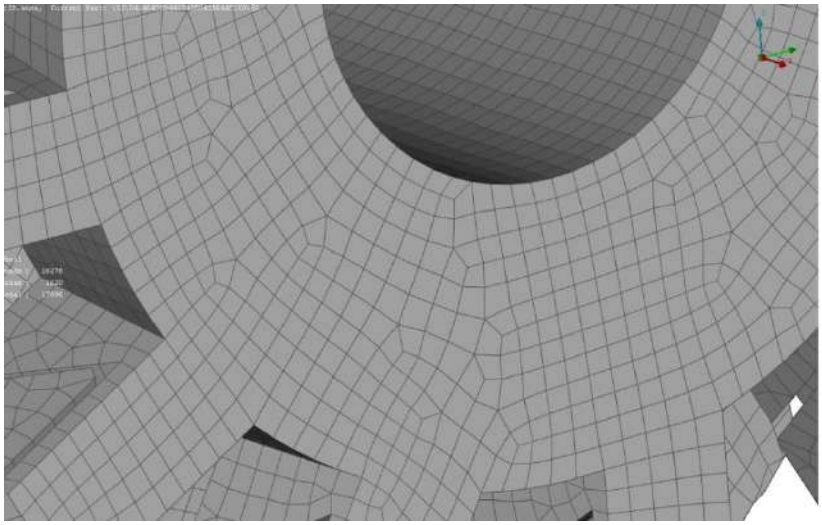

**Fig. 1.** – Finite element mesh

Presenting the simulation modeling methodology in the form of a certain sequence, we can distinguish 7 main steps.

At step 1 (Step 1 - material properties) are specified by the input data for the designed design of a prefabricated cutter for dimensional processing of splines. In order to obtain a stress state of the cutter close to real milling conditions, a dynamic load mode was used, taking into account the data indicated in Table 1.

**Table 1.** Loads during operation of a milling cutter with replaceable inserts

| Parameter name | Meaning |
|---|---|
| Axial feed of milling cutter | 52.3 mm/rev |
| Feed per tooth | 0.06 mm |
| Cutting speed | 638 m/min |
| Rotation frequency | 82 rpm |

Also, to simulate the stress state, the properties of materials were determined - this is the material of the cutter body, replaceable carbide inserts (Table 4.2).

**Table 2.** Physical properties of materials involved in the process of milling the machined surface

| Physical parameter of the material | Milling cutter body material - steel 30KhGSA (GOST 4543) | Plate material – T5K10 (GOST 3882) |
|---|---|---|
| Density | 7.85 g/cm$^3$ | 12.5-13.1 g/cm $^3$ |
| Poisson's ratio | 0.280 | 0.21 |
| Tensile strength | 820 MPa | 1421 MPa |
| Yield strength | >835 MPa | - |
| Elongation at break | >10% | - |
| Volume modulus of elasticity | 215 GPa | 160 GPa |
| Shear modulus | 84000 MPa | 245× 10$^9$ Pa |

To determine point stress amplitudes, the following scheme was used (Figure 2).

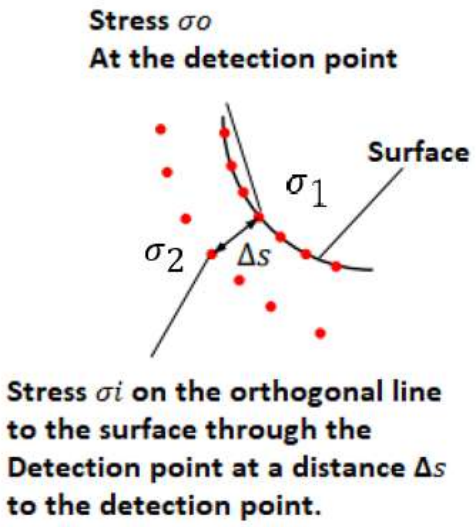


**Fig. 2.** – Diagram of point stress amplitudes

At the second stage (2 Step (Temperature factor)), the working temperature was selected, T = 1200ºC. The choice of such a high value is explained by the fact that the mechanical processing of materials of increased hardness and strength requires significantly more energy, which leads to an increase in temperature in the cutting zone, which can reach 1100 °C. Accelerating the processing process, including increasing the tool feed, also leads to a significant increase in the amount of heat in the processing zone [10].

At the third stage (3 Step (Construction characteristics), to analyze the fatigue strength and the nature of the distribution of internal stresses of the samples, a calculation technique was used [11], according to which readings of the internal stress characteristics are taken from two points, taking into account the distance between them, and the gradient was also calculated stress.

When modeling, amplitude (alternating) loads were chosen as loads on the cutter, since they are the worst for any model.

The fatigue strength of materials under repeated variable loading largely depends on the nature of the change in stress over time.

The place where the loads are applied is the area surrounding the cutting edge of the cutter, simulating roughing with a cutting depth of 2 mm.

At the fourth stage (4 Step (amplitude initialization)), the program automatically determined the loads for the designed cutter structure based on the entered input parameters.

Periodic load is a variable load with a pattern of change established over time, the values of which are repeated after a certain period of time. The determination of voltage values is graphically presented in Figure 3.

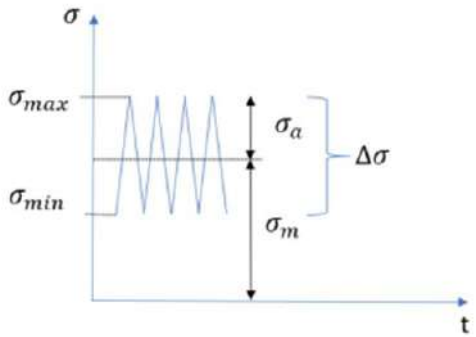


**Fig. 3.** - Stress cycle

Stress cycle is the totality of all alternating stress values during one period of load change.

Typically, the stress cycle is characterized by two main cycle parameters:

– $\sigma_{max}$ - maximum cycle stress;

– $\sigma_{min}$ - minimum cycle stress;

– $\sigma_m$ - average cycle stress [11].

The amplitude cycle stress is determined by the formula [11]:

$$\sigma_a = \frac{\sigma_{max} - \sigma_{min}}{2} \quad (1)$$

The average cycle stress is determined by the formula [11]:

$$\sigma_m = \frac{\sigma_{max} + \sigma_{min}}{2} \quad (2)$$

where $\sigma_{max}$, $\sigma_{min}$ – maximum and minimum values of equivalent stresses.

The stress cycle asymmetry coefficient is determined by the formula [11]:

$$R = \frac{\sigma_{max}}{\sigma_{min}} \quad (3)$$

In cyclic loading, during alternation, the average stresses are equal to 0, and during pulsations, the average stresses are equal to the amplitude stresses (Figure 4).

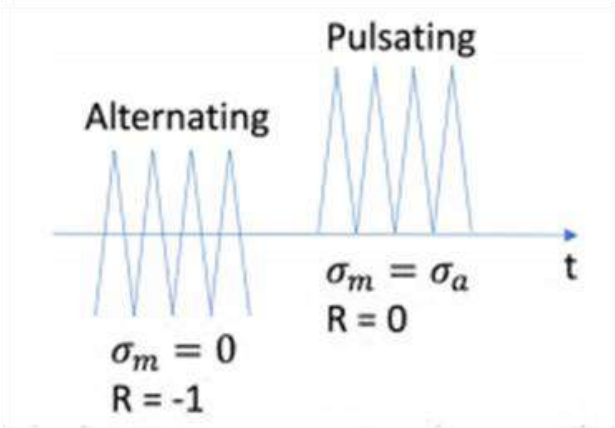


**Fig. 4. -** Stress coefficients for alternations and pulsations

The overall safety factor is determined by the formula [11]:

$$\alpha_{BK,\sigma} = \frac{\sigma_{\alpha 1}}{\sigma_{BK}} \cdot j_D \quad (5)$$

where $\sigma_{a,1}$ – maximum stress amplitude depending on the type of stress, MPa;

$\sigma_{BK}$ - fatigue strength of components, MPa;

$j_D$ - overall fatigue strength coefficient.

The overall fatigue strength coefficient is determined by the formula [11]:

$$j_D = \frac{j_F}{k_{td}} \cdot j_s, \quad (6)$$

where $j_F$ – material safety factor;

$j_s$ – safety factor ($j_s$ = 1 with an average probability of maintaining the safety margin 97,5%);

$k_{TD}$ – temperature coefficient ($K_{TD}$ = 1 for alloy steel).

**2. Results and discussion**

Based on the results obtained, the sensitivity of the model to amplitude loads, as well as the fatigue strength of the components, were calculated. The results of calculating the distribution of internal stresses are presented in Table 3.

**Table 3.** Propagation of internal stresses as a result of milling cutter simulation

| Input data | |
|---|---|
| Maximum stress, $\sigma_{max}$, MPa | 326 |
| Minimum stress, $\sigma_{min}$, MPa | 32 |
| Intermediate results | |
| Amplitude cycle stress, $\sigma_a$, MPa | 147 |
| Stress cycle asymmetry coefficient, R | 0.0981595 |
| Stress sensitivity, $M_\sigma$ | 0.417 |
| Medium stress factor, $K_{AK,\sigma}$ | 0.68745351 |
| Average cycle stress, $\sigma_m$, MPa | 179 |

Maximum stress ($\sigma_{max}$ = 326 MPa) is the stress that occurs in the cutter body, where the replaceable carbide insert meets, which occurs when the cutter tooth enters the workpiece. This leads to a sharp change in the cross-sectional area of the cut, and, consequently, in the forces acting during the cutting process.

Minimum stress ($\sigma_{min}$ = 32 MPa) this is the stress considered in the same place, which remains in the cutter body from the moment the cutter tooth leaves the machined surface and makes a circle until the next entry into the workpiece, the so-called residual stress.

The amplitude cycle stress ($\sigma_a$ = 147 MPa) was obtained using formula (1).

At the fifth stage (5 Step (Work cycles)), the strength of the cutter was investigated. To simulate the operation of the cutter during the cutting process, the "dynamic mode" was used. Dynamic loads include periodic, repetitive (cyclic) loads. When modeling the cutter, the average value of the load cycles of the cutter structure $4\times10^6$ acting on the structural elements was specified. with given conditions. As practice shows, loads that change cyclically over time in magnitude or in magnitude and sign can lead to the destruction of a structure at stresses significantly lower than the yield strength (or tensile strength). This kind of failure is usually called "fatigue". The results are presented in Table 4.

**Table 4.** Influence of the number of working cycles on the strength of the cutter structure

| Input data | |
|---|---|
| Number of cycles (default number of work cycles $4\times10^6$) | |
| N | 4000000 |
| Intermediate results | |
| Fatigue coefficient, $K_{BK}$ | 1 |
| Fatigue Strength of Components,$\sigma_{BK}$, MPa | 234.705358 |

With a given endurance limit for steel 30XGSA = 490 MPa, the proposed cutter design is able to resist fatigue failure, since $\sigma_{вк}$ = 234.705358 MPa.

According to the ISO 15641 standard, safety requirements are established for high-speed processing (mechanical removal of chips at high peripheral speeds) on metal-cutting machines as a result of the use of cutters. ISO 15641 establishes design methods, centrifugal force test procedures, operational limitations and provides information to minimize or eliminate these hazards. Therefore, at the sixth stage (6 Step (safety factor)), the worst-case operating conditions of the cutter with the imposition of large amplitude loads and a high degree of wear were investigated (Table 5).

**Table 5.** Results of operating the cutter with high amplitude loads

| Input data | |
|---|---|
| Material safety factor, $j_f$ | 1.2 |
| Final results | |
| Overall fatigue strength factor, $j_D$ | 1.26758151 |
| Overall safety factor, $\alpha_{BK,\sigma}$ | 0.79390809 |

According to Table 5, we can conclude that the safety factor of the material is 1.2. It is the lower limit of the standard safety factor of the material (1.2÷1.5) [12]. It was also found that under the action of amplitude loads during 4×106 loading cycles, the overall safety factor is equal to 0.79390809 MPa. This means that the assembled milling cutter in question with replaceable inserts has a damage resistance reserve level of about 20% and remains operational.

In addition to fatigue strength, the study identified stress concentrators of a milling cutter with replaceable inserts during the cutting process (Figure 5).

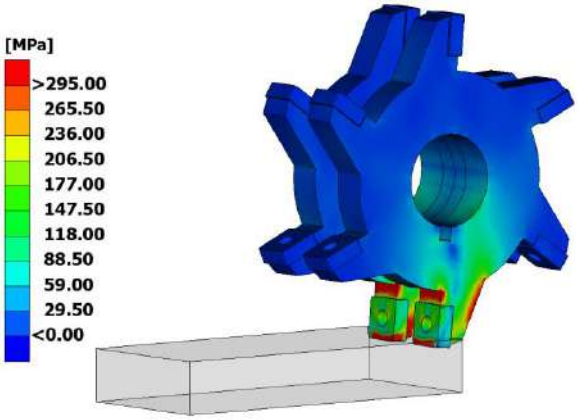


**Fig. 5.** - Stresses in a milling cutter with replaceable inserts during the cutting process

According to the data obtained, the highly loaded surfaces of the assembled cutter with replaceable plates are the step transition of the cutter teeth, the stresses on which are 296 - 298 MPa (Figure 6), and the rear part of the teeth, the stresses on which are 295 - 296 MPa.

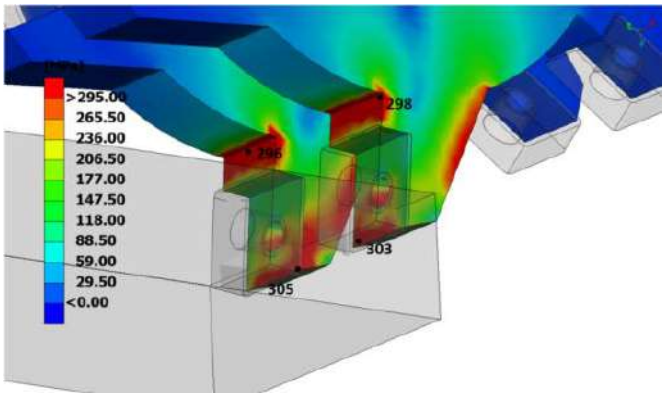


**Fig. 6.** – Stresses in stepped transitions of cutter teeth

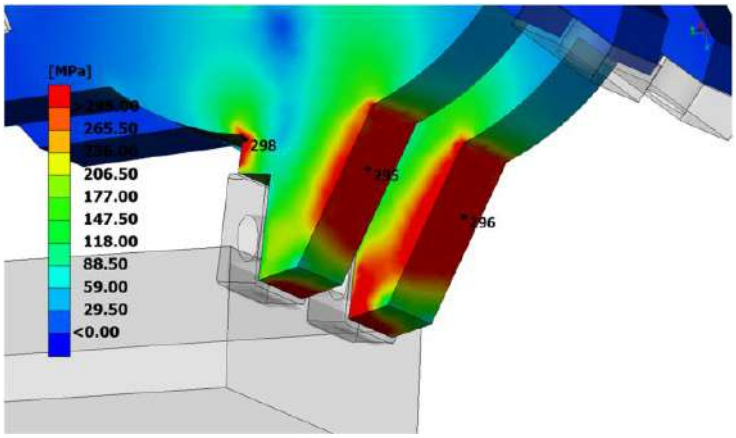


**Fig. 7.** – Stresses on the back of the cutter teeth

The highest stresses (345 – 365 MPa) in the cutter design occur at the edges of the replaceable inserts, since they have direct contact with the material being processed during machining (Figure 8).

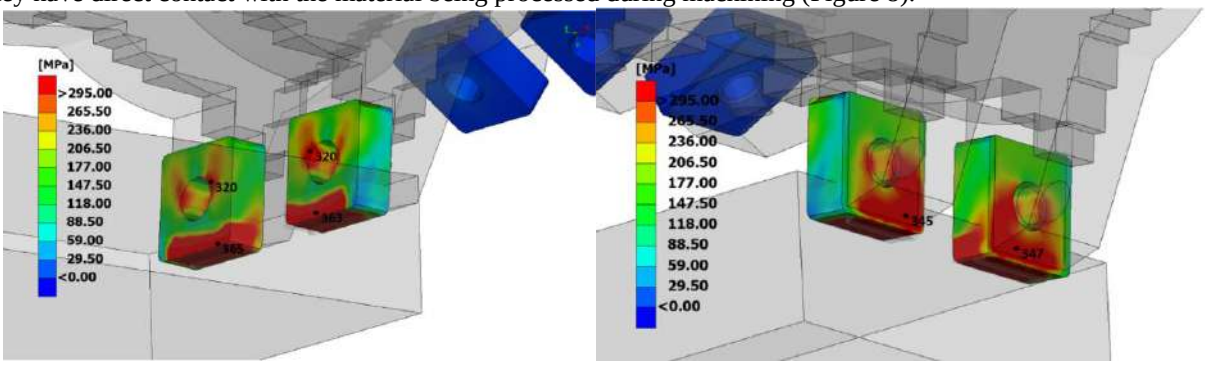


**Fig. 8.** - Stresses on the replaceable inserts of a prefabricated cutter

In this area, scratches and chipping of the cutting edge of the insert will form on the rake surface, reducing the strength of the cutting edge. Accordingly, the greatest wear on the rake surface will occur precisely in this zone, since it is in this area that the greatest cutting constraint is observed.

Also, the vulnerable point of the plate is the circular cross-section for mechanical fastening, the stress in which is 320 MPa.

To evaluate the structural strength of a prefabricated milling cutter with replaceable inserts, the stress concentration coefficient and the strength coefficient were used.

The safety factor is determined by formula (6):

$$n = \frac{\sigma_t}{\sigma_{max}} \quad (6)$$

where $\sigma_t$ – yield strength of the material, MPa;

$\sigma_{max}$ - maximum stress in the milling cutter, MPa.

The results of the study of the stress state of a cutter assembly with replaceable inserts are presented in Table 4.6.

**Table 6.** Parameters of the stress state of a cutter assembly with replaceable inserts

| Parameter name | Parameter value in stepped tooth transitions | Parameter value for the back side of the teeth | Parameter value for replaceable inserts |
|---|---|---|---|
| Maximum stress, MPa | 298 | 296 | 365 |
| Safety factor | 1.5 | 1.5 | 4.9 |

The standard safety factor for cutting tools in mechanical engineering is $n \geq (1.5 \div 2.5)$ [13]. The safety margin is maintained for all components of the cutter design, with a stress spread of 60 MPa, provided that extra loads were specified that exceeded the actual loads by 4 times. However, for replaceable plates the safety margin is higher since they are made of high-alloy T5K10 glory, consisting of chromium, tungsten and vanadium.

Thus, as a result of assessing the strength of the design of a cutter assembly with replaceable plates during machining, it was established that the design has a 20% margin of fatigue strength and can be used when processing spline surfaces of parts such as rotating bodies.

**Conclusions**

1. The developed strength assessment method determines the amplitude cycle stress, cycle asymmetry coefficient, sensitivity, average stress factor, average cycle stress, fatigue strength and fatigue strength coefficient, as well as the safety factor of the structure.

2. The safety factor of replaceable polyhedral inserts is 3 times higher than the safety factor of the cutter body.

3. Dangerous stress concentrators of a cutter assembly with replaceable inserts are the stepped transitions and the back side of the teeth, the circular section for mechanical fastening, as well as the cutting edge of replaceable multifaceted inserts.

4. The design of the prefabricated cutter with replaceable inserts satisfies the standard safety factor, which allows its use when processing deposited surfaces.

**References**

[1] Choudhury S.K., Bajpai J.B. Investigation in orthogonal turn-milling towards better surface finish //Journal of Materials Processing Technology, Volume 170, Issue 3, 2005. - P. 487 - 493

[2] Equeter L., Ducobu F., Dehombreux P. Cutting Tools Replacement: Toward a Holistic Framework //IFAC-PapersOnLine, Volume 53, Issue 3, 2020. - P. 227 - 232

[3] Jagota, V., Singh, A., Amanpreet S., Singh Sethi, Kumar Dr-Kh. Finite Element Method: An Overview //Walailak Journal of Science and Technology (WJST), 10(1), 1-8

[4] Holland I. Fundamentals of the finite element method //Computers & Structures, Volume 4, Issue 1, 1974. - P. 3-15

[5] Erhunmwun I., Ikponmwosa U. Review on finite element method //Journal of Applied Sciences and Environmental Management, 21(5), 2017, P. 999

[6] Cen S., Li C., Rajendran S., Hu Zh. Advances in Finite Element Method //Mathematical Problems in Engineering, Volume 2014, P. 1 - 2

[7] Zharkevich O., Nikonova T., Gierz Ł., Berg A., Berg A., Zhunuspekov D., Warguła Ł., Łykowski W., Fryczy ´nski K. Parametric Optimization of a New Gear Pump Casing Based on Weight Using a Finite Element Method //Applied Science 13, 2023, P. 12154.

[8] Wei-Hai Yuan, Hao-Cheng Wang, Wei Zhang, Kang Liu, Yuan Wang Particle finite element method implementation for large deformation analysis using Abaqus //Acta Geotechnica, 2021, 16(12), P. 1-14

[9] Shun Chen Introduction study on the influence of residual stress on contact stiffness of joint surface //J. Phys.: Conf. Ser. 2553, 2023, P. 012031

[10] Tempelman E, Shercliff H., Eyben B. Manufacturing and Design Understanding the principles of how things are made. Chapter 7 – Machining, 2014, P.105-120

[11] Roland Rennert, Eckehard Kulling. Rechnerischer Festigkeitsnachwe1s fur Mas-chinenbauteile aus Stahl, Eisenguss- und Aluminiumwerkstoffen. Herausgeber: Forschungskuratorium Maschincnbau (FKM), 2020. – 230 p.

[12] J. Carvill Mechanical Engineer's Data Handbook, 8 - General data , 1993, P. 288-310

[13] Rawlings J., Pantula S., Dickey D. Applied Regression Analysis a Research Tool Textbook Springer Texts in Statistics (STS); Berlin/Heidelberg: Springer, Germany, 1998, 456 p.

**Information of the authors**

**Nurzhanova Oxana Amangeldyevna**, master, senior teacher, Abylkas Saginov Karaganda Technical University
e-mail: nurzhanova_o@mail.ru

**Zharkevich Olga Michailovna**, c.t.s., professor, Abylkas Saginov Karaganda Technical University
e-mail: zharkevich82@mail.ru

**Berg Andrey Alexeyevich**, master, assistant, Abylkas Saginov Karaganda Technical University
e-mail: 22526633@mail.ru

**Zhukova Alla Valentinovna**, senior teacher, Abylkas Saginov Karaganda Technical University
e-mail: aluny@mail.ru

**Mussayev Medgat Muratovich**, PhD, ass.professor, Abylkas Saginov Karaganda Technical University
e-mail: kstu_mmm@mail.ru

**Buzauova Toty Meyerbekovna**, c.t.s, ass.professor, Abylkas Saginov Karaganda Technical University
e-mail: toty_77@mail.ru

**Abdugalieva Gulnur Baymurzaevna**, c.t.s, ass.professor, Abylkas Saginov Karaganda Technical University
e-mail: gulnura84@mail.ru

**Shakhatova Aliya Talgatovna**, PhD candidate,senior lecturer, Abylkas Saginov Karaganda Technical University
e-mail: shakhatovaa@list.ru

**DOI 10.52209/2706-977X_2023_4_18 IRSTI 55.09.99 UDC 621.373.826:533.9**

# Modification of Polypropylene Films by Laser Radiation

**Shupan P., Gavrilova V.*, Mussafirova G.**
Yanka Kupala Grodno State University, Grodno, Republic of Belarus
*corresponding author

**Abstract**. In work the effect of laser radiation on the structure, surface activity and tensile strength of polypropylene films is investigated, which is confirmed by IR spectroscopic studies. As a result of experimental studies of the contact angle of wetting after laser irradiation of the studied samples, changes in their surface activity were observed: with an increase in the density of laser radiation with a power of up to $1.63\times10^5$ W/cm$^2$, the contact angle of wetting decreases, the highest values of the studied parameter are observed in a film irradiated with a power of $2.26\times10^5$ W/cm$^2$. Analyzing the results of strain- strength tests, it can be concluded that after laser treatment, the tensile strength of films increases, while the highest strength and elongation value are observed in a sample irradiated with a laser with a power density of 2.26 × 105 W/cm$^2$. The work shows that the physical and mechanical characteristics of polypropylene films depend on the modes of laser radiation, the optimal results of the studied indicators are achieved with laser irradiation with a power density of $2.26 \times 10^5$ W/cm$^2$.

**Keywords:** laser radiation, polypropylene films, modification, surface activity, supramolecular structure.

**Introduction.**

Laser radiation affects the chemical construction, structure, physico-chemical and physico-mechanical properties of polymer materials. Effects associated with changes in crystallinity, morphology, hardening and formation of a certain charge state of the surface layer are observed. The nature of the exposure is primarily determined by the irradiation modes. Lasers with different wavelengths of radiation in the range from near-ultraviolet to far-infrared are widely used to modify polymers. The ability to adjust the parameters of laser processing in a wide range of modes allows you to adjust the structure of the surface layer and its properties, such as hardness, wear resistance, roughness, etc.

The energetic activation of the surfaces of polymeric materials by laser action leads to an increase in operational properties. Activated surfaces acquire new qualities due to the removal of adsorbed low molecular weight products and contaminants from them [1,2].

The purpose of this research is to study the peculiarities of changes in the supramolecular structure, durability and surface activity of polypropylene films subjected to laser irradiation.

**1. Research methodology**

As a material for the study, there were used a polypropylene (PP) film of the BOPP STT brand 0.020 × 105 TU RB 00204079.164-97 produced by JSC Mogilevkhimvolokno and a film of the BOPP STT brand 0.020 × 105 TU RB 00204079.164-97 produced by Irplast.

The samples were irradiated using an YAG laser with a radiation wavelength of λ = 532 nm with power densities of $q_1 = 1{,}01\times10^5$ W/cm$^2$; $q_2 = 1{,}63\times10^5$ W/cm$^2$; $q_3 = 2{,}26\times10^5$ W/cm$^2$; $q_4 = 2{,}77\times10^5$ W/cm$^2$.

The designations of the samples are given in Table1.

**Table1**. Designations and interpretation of test samples

| Sample designation | Interpretation of sample designation |
|---|---|
| I.1 | PP of the JSC Mogilevkhimvolokno brand |
| I.2 | PP of the JSC Mogilevkhimvolokno brand, irradiated with laser radiation with a power density of $q_1 = 1{,}01\times10^5$ W/cm$^2$ |
| I.3 | PP of the JSC Mogilevkhimvolokno brand, irradiated with laser radiation with a power density of $q_2 = 1{,}63\times10^5$ W/cm$^2$ |
| I.4 | PP of the JSC Mogilevkhimvolokno brand, irradiated with laser radiation with a power density of $q_3 = 2{,}26\times10^5$ W/cm$^2$ |
| I.5 | PP of the JSC Mogilevkhimvolokno brand, irradiated with laser radiation with a power density of $q_4 = 2{,}77\times10^5$ W/cm$^2$ |
| II | PP of the Irplast brand |

The adsorption properties of the films were evaluated by the contact angle of wetting in accordance with GOST 7934.2-74. The tensile strength was determined on a breaking machine model RM-30-1 according to GOST 14236-81. The morphology and topography of the surface of the films were studied using an atomic force microscope NANOTOP-206. The surface structure of the samples was studied by infrared spectroscopy. The studies

were carried out on an ALPHA spectrometer. Identification and analysis of IR spectra were carried out according to known methods using data on IR spectra of polymer materials [3].

**2. Results and discussion**

The obtained absorption spectra are shown in Figure1.

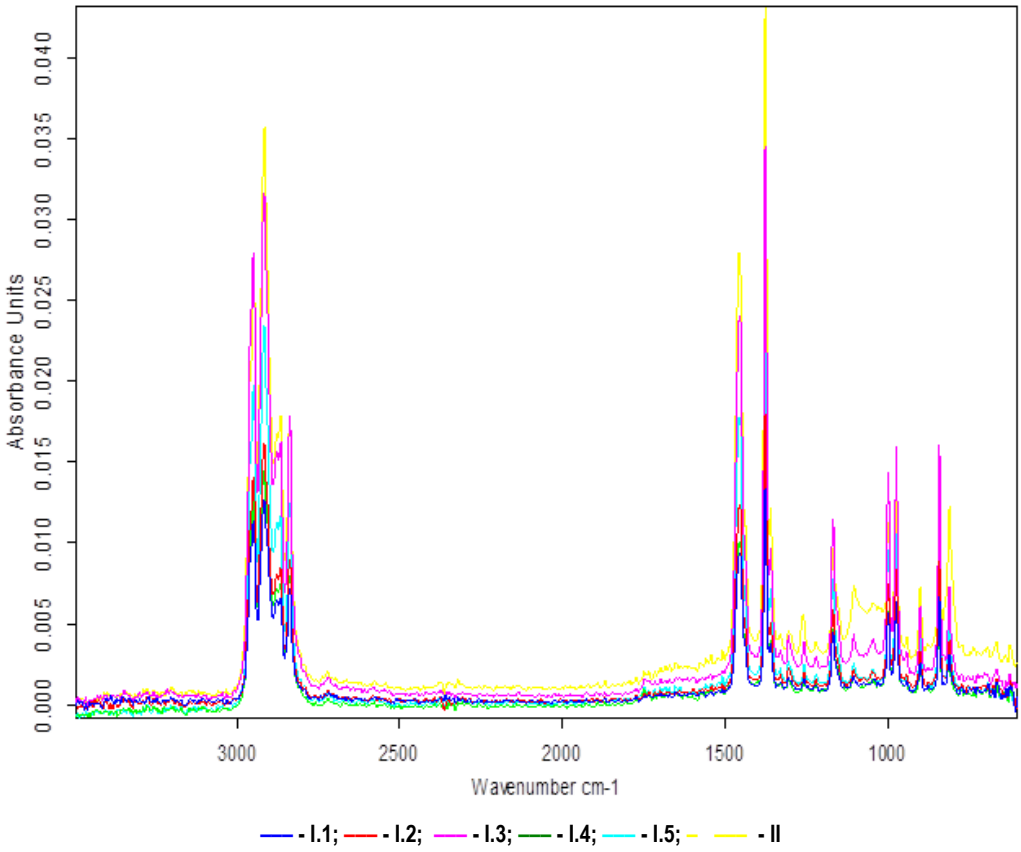


**Fig. 1.** – IR spectra of the studied samples in the far-infrared region

IR spectroscopic studies have shown that after laser irradiation, the structure and phase state of the substance in the samples under study change. Signs of structural transformations of polypropylene film samples are: redistribution of groupings with C-C bonds (790 $cm^{-1}$); change in the intensities of a number of absorption bands at 1455 $cm^{-1}$ and 1375 $cm^{-1}$ (deformation vibrations of $CH_3$ groups in trans-conformations); 2920 $cm^{-1}$ and 2838 $cm^{-1}$ (valence fluctuations of CH and $CH_2$ groups in trans-conformations); as well as the redistribution of the intensities of the absorption bands in the area corresponding to the transparency zone (1500 $cm^{-1}$ – 2600 $cm^{-1}$) [4].

Structural changes in the surface layers of polypropylene films cause another important effect – a change in surface activity, estimated by the value of the contact angle of wetting.

Table 2 shows the values of the contact angle of wetting of polymer films.

**Table 2.** Values of the contact angle of wetting of polymer films

| Sample designation | I .1 | I .2 | I .3 | I .4 | I .5 | II |
|---|---|---|---|---|---|---|
| Values of the contact angle of wetting θ, grad | 55 | 43 | 46 | 59 | 40 | 43 |

Analysis of the data in Table 2 showed that the smallest wetting angle is observed in the initial sample of the Irplast brand. The surface tension of BOPP STT films after irradiation varies ambiguously: with an increase in the power density to 1.63 ×105 W/$cm^2$, the contact angle of wetting decreases and then increases, its highest value is observed in the irradiated film with a power density of 2.26×105 W/$cm^2$. The surface of all films is hydrophilic, because the contact angle of wetting $\theta$ is less than 90 degrees [5].

The results of deformation and strength tests are presented in Figures 2,3

As a result of stress-strain tests, it was found that after laser treatment, the tensile strength of films increases. The highest strength and elongation value are observed in a sample exposed to radiation by the laser a power density of which is 2.26×105 W/$cm^2$. With a further increase in the power density of the laser radiation, the strength of the films decreases

As a result of scanning the surface of the films with an atomic force microscope, AFM images of the microrelief were obtained in the phase contrast mode (a), as well as in the topography mode (b). The test results are shown in Figure 4.

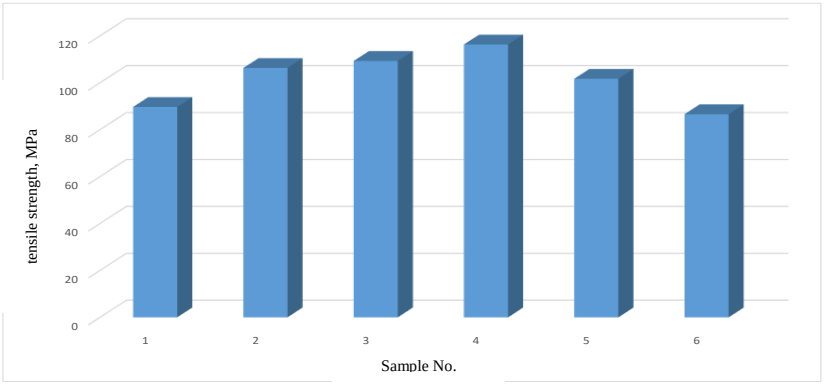


**Fig. 2. –** Values of the tensile strength of films

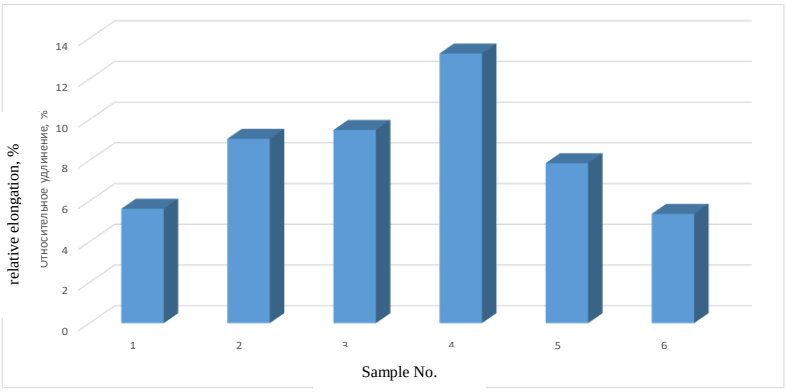


**Fig. 3.** – Values of relative elongation of samples

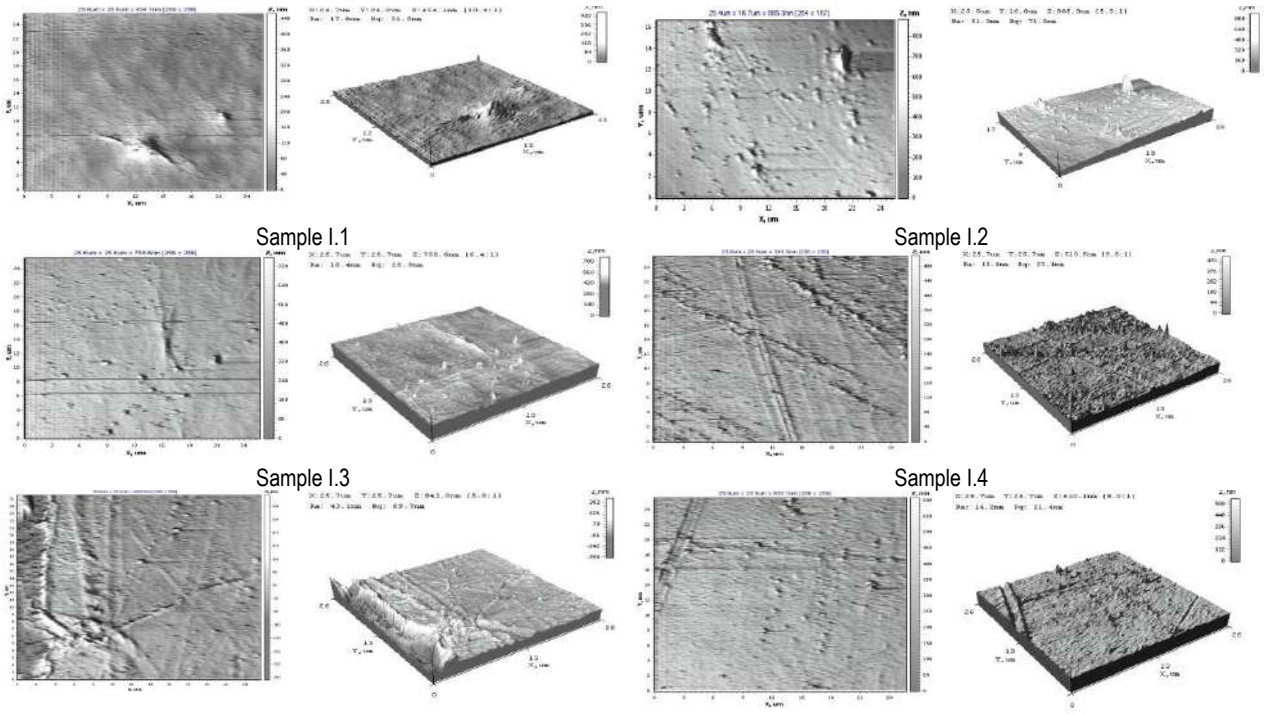


a) – AFM-image in phase contrast mode; b) – AFM -image of microrelief in topography mode

**Fig. 4. –** Morphology and topography of the surface of samples

Analyzing the results of atomic force microscopy, it was found that the shape and structure of the film surface changes under the influence of laser irradiation. The surface of the initial film (sample II) is smoothed, single protrusions are observed. When exposed to laser irradiation, the surface of the films (samples I.1, I.2, I.3) acquires a more structured, ordered form. During irradiation of the film (sample I.4) with a laser irradiation power density of 2.26×105 W/cm$^2$, a cluster structure is formed on the surface. With a further increase in the power density to 2.77 ×105 W/cm$^2$, microcracks and micro-depressions are observed on the surface of the films. It should be noted that the results of atomic force microscopy correlate with the results of deformation and strength tests [6].

## Conclusions

Based on the results obtained, it can be concluded that high-energy processing of polypropylene films leads to a transformation of the supramolecular structure and a change in surface activity and, as a consequence, to a change in the deformation and strength characteristics of polypropylene films. Thus, with the help of laser irradiation, it is possible to directionally change the structure of polymer films in order to improve their service characteristics. Optimal physical and mechanical characteristics of the studied samples are achieved by laser irradiation with a power density of 2.26 × 105 W/cm$^2$.

**References**

[1] Gavrilova V.V. Investigation of the structure and mechanical properties of polymer films irradiated by laser radiation / V.V. Gavrilova, P.I. Shupan, I.G. Sergienko // Modern problems of polymer science: collection of abstracts of the International Conference, Tashkent, November 14, 2016 – Tashkent: SIC Chemistry and Physics of Polymers, 2016, P. 128-130.
[2] Sarokin V.G. Technology of laser modification of polymer semi-finished products for applying decorative coatings / V.G. Sorokin, E.I. Eissymont, E.V. Novogrodskaya, A.V. Chekel // Interaction of Radiation with Solids = Взаимодействие излучений с твердым телом: Proceedings of the 9th International Conference, September 20-22, 2011. Section 6. Equipment and technology. – Minsk, 2011, P. 453-455.
[3] Infrared spectroscopy of polymers; edited by I. Dehant. – M.: Chemistry, 1972. – 472 p.
[4] Sarokin V. Technology laser modification in material science nanocomposites for Metal-Polymeric systems // Innovations in engineering : proceedings of IInd international scietific conference, Varna, Bulgaria, 20-23 june 2016 / Scientific proceedings of the scientific-technical union of mechanical engineering. - Bulgaria, Sofia, 2016, P. 64-65.
[5] Sarokin V. Laser technology in materials science nanocjmposite materials based on thermoplastics / V. Sarokin, S. Avdeychik, V.Struk // Scientific technical journal "Materials Science", Bulgaria, Sofia, 2015, P. 51-54.
[6] Yarmolenko M.A. Features of degradation of polymer materials under the influence of short-wave laser radiation / M.A. Yarmolenko, A.A. Rogachev, Imin Liu, A.V. Rogachev, Lihong Gao, Zhua Ma // Scientific and Technical Journal "Problems of Physics, Mathematics and Technology", Physics. – No. 1 (50), 2022, P. 49-54.

**Information of the authors**

**Shupan Pavel Ivanovich,** master of engineering sciences, senior lecturer, Yanka Kupala State University
e-mail: shupan_pi@grsu.by

**Gavrilova Valentina Vladimirovna,** master of engineering sciences, senior lecturer, Yanka Kupala State University
e-mail: v.gavrilova@ grsu.by

**Mussafirova Galina Yaroslavovna,** candidate of technical sciences, associate professor, Yanka Kupala State University
e-mail: musafirova_gy@grsu.by

**DOI 10.52209/2706-977X_2023_4_22 IRSTI 53.49.17 UDC 669.168**

# Study of the Influence of the Composition of Manganese Ores on the Quality of Silicomanganese

**Naboko E.P., Issagulova D.A.*, Platonova E.S., Yudakova V.A., Pitirimova T.V.**
Abylkas Saginov Karaganda Technical University, Karaganda, Kazakhstan
*corresponding author

**Abstract:** Today the production of silicomanganese is in a promising direction. Silicon manganese is used to alloy steels, increasing their strength and corrosion resistance; in the production of cast iron, where it plays the role of a desulfurizer and degasser. In recent years, the demand for silicomanganese has increased significantly, which is caused by an increase in steel production in the world. In this work, the issue of using "poor" manganese ores of Kazakh origin to produce high-quality ferroalloys with reduced costs (by reducing import logistics costs) based on Kazakh enterprises was investigated.

**Keywords:** silicomanganese, manganese ore, raw materials, alloy, steel, cast iron, ferroalloy, mineral composition, phosphorus, chemical composition.

## Introduction

The mining and metallurgical complex of the republic is one of the basic industries that plays an important role in the formation of the country's macroeconomic indicators. The development of the national economy as a whole will depend on its further development.

Currently, the goal of Kazakhstan's industrial policy is to create the most balanced industrial complex (industrial-innovative), capable of serving the domestic market with competitive products for further processing, constantly increasing export potential through highly processed products.

Ferroalloys, which until recently were a semi-product of metallurgical production, are today used not only as an alloying additive but also in the production of various products and structures. Silico-manganese is used to degas the steel, reduce the exposure of the metal alloy to sulfur and phosphorus, and provide increased strength and wear resistance to the steel. In addition, it can be used in the production of electrodes, other types of ferroalloys, casting alloys and other metal products.

Ferroalloy production is a relatively new branch of metallurgy in Kazakhstan. Until recently, it was represented by two large factories located in Aksu and Aktobe, owned by JSC Transnational Company Kazchrome. Both plants specialize in the production of such types of alloys as ferrosilicon, ferrochrome and silicomanganese.

Kazakhstan occupies one of the leading places in the ranking of producers of these types of alloys and is also one of the largest exporters. Considering ferroalloy production in the Commonwealth of Independent States countries recently, it can be noted that 25 ferroalloy plants produce about 4.8 million tons of finished products per year. A feature of the production of ferroalloys is the fourfold excess of product production over domestic consumption in metallurgical production, which explains that this production is mainly export-oriented

The Karaganda region became a center of ferroalloy production relatively recently. Today, in the industrial zone of the city of Karaganda there are two ferroalloy plants, YDD Corporation LLP and Asia FerroAlloys LLP. The enterprises produce high-quality ferrosilicon (an alloy of iron and silicon). The Asia FerroAlloys LLP company specializes in the production of silicomanganese of the MnC17 grade. Product output is aimed at meeting local and global demand for ferroalloys in the markets of Kazakhstan, Europe, Southeast Asia, North and South America. The enterprises' products meet the highest international quality requirements.

## 1. Research methodology

When assessing the quality of ores, the first place comes the question of the content of the main element in them, but this criterion also changes. Due to the increasing depletion of minerals, consumers are now settling for increasingly poorer minerals. When deciding on the use of a particular grade of ore in production, the technical and economic results of work on this ore should be assessed. In this case, first of all, it should be taken into account that reducing the proportion of manganese in the charge by 1%, other things being equal, reduces the furnace productivity by 2.3%. A decrease in the $Cr_2O_3$ content in the ore by 1% reduces the productivity of the furnace and, accordingly, increases energy consumption in the production of low-carbon ferrochrome by 4.8% and high-carbon ferrochrome by 3%. The value of ore increases by reducing the content of harmful impurities such as phosphorus, sulfur and copper [1].

The number of impurities often determines the processing technology. The volumes of Kazakhstani manganese ores mined for the production of silicomanganese make it possible to meet the needs of the growing ferroalloy production of the metallurgical industry of Kazakhstan. The main advantage of domestic manganese raw materials is its low phosphorus content, which ensures the production of low-phosphorus ferroalloys; silicomanganese with phosphorus content of less than 0.15% and ferromanganese carbon of less than 0.25%. This allows the use of raw materials without preliminary preparation - enrichment [2].

Kazakhstan occupies one of the leading positions among the Commonwealth of Independent States countries in terms of manganese ore reserves. Today, about 100 manganese deposits are known on the territory of the Republic, 19 of them are included in the country's balance sheet. Manganese ores in Kazakhstan are classified into three main groups:

Zhezdy -Ulutau, Atasu and Ushkatyn. Manganese ores of the first group are characterized by low manganese content (15 - 17%) and high silica content (40 - 49%). Deposits of manganese ores of the Atasu group: Western Karazhal, Ushkatyn I, Ushkatyn III, Tur, Zhomart, Kamys, Bogach, Zhaksy, Akzhar-Sarytuma and other manganese deposits are concentrated almost exclusively in Central Kazakhstan.

In the process of work, studies were carried out on the influence of the composition of manganese ores on the quality of the resulting ferroalloy. Two deposits were considered: with a low mass fraction of the leading element content and with a high one. These are the Zhezdy deposit and the Akzhar-Sarytum deposit, respectively.

Manganese ores with a leading element content of 22.5 - 38% are mined in the Akzhar-Sarytuma deposit (Table 1), located on the border of the Karaganda and Zhambyl regions. Manganese ores are concentrated in the northern part of the deposit. Ore deposits are confined to the very bottom of the section and are usually represented by interlaying of red-colored conglomerates, gravesites, sandstones and peroxide ores. Mineral composition of the ores: braunite, psilomelane, pyrolusite. The greatest thickness of the ore-bearing horizon (up to 50 m) was noted at the Akzhar-Sarytuma deposit. In other places, it usually does not exceed 10 m.

**Table 1.** Chemical composition of manganese ore from the Akzhar-Sarytuma deposit

| Mn | Fe | $SiO_2$ | MgO | $Al_2O_3$ | CaO | P |
|---|---|---|---|---|---|---|
| 38,7% | 3,2% | 23,5% | - | - | 3,4% | 0,002% |

Zhezdy ores (Table 2) with an average manganese content of 17% are characterized by a low phosphorus content and a high silica content. Ores fall into the category of dense, hard and refractory ores. Concentrates containing more than 45% manganese can only be obtained by fine grinding (up to 0.15 mm) and using complex enrichment schemes. Also, these ores contain tenths of a percent of lead, hundredths of copper and titanium, thousandths of cobalt, molybdenum, and thallium. Barium is present (average 2.36% BaO). This deposit of manganese ores has approved reserves of about seven million tons, which are in reserve.

**Table 2.** Chemical composition of manganese ore from the Zhezdy deposit

| Mn | Fe | $SiO_2$ | MgO | $Al_2O_3$ | CaO | P |
|---|---|---|---|---|---|---|
| 16,6% | 4,75% | 46,5% | 0,6 | 10,2 | 2,51% | 0,022% |

The main iron-containing component of the charge when melting silicon alloys is carbon steel fragments. The use of scrap ferrous metals is permitted only when melting alloys intended for use in iron foundries. This is due to the fact that phosphorus (>1.2%) contained in scrap ferrous metals is almost completely converted into an alloy. The use of scrap ferrous alloys or scrap contaminated with impurities of non-ferrous metals is not permitted. An exception, however, is the use of chromium steel scrap for the production of alloys containing chromium, etc. The use of long and tangled iron shavings, which impede portion feeding, as well as scrap contaminated with a large amount of oil and oxidized iron scrap, is not allowed. The use of highly oxidized scrap increases the consumption of energy and reducing agents, and scrap containing iron oxide hydrides also increases the hydrogen content of the alloy [3].

Repeated attempts to use iron ore or scrap iron instead of shavings in the restoration process were unsuccessful. In this case, to reduce iron oxide, it is necessary to increase the carbon content in the charge by approximately 20 kg per 100 kg of ore, which negates the expected improvement in the electrical resistance of the charge or the depth of the electrode. In addition, even good- quality ore contains 13 kg of slag-forming impurities per 100 kg, which leads to the conclusion that it is inappropriate to use ore (or iron ingots) in the reduction process for the production of ferroalloys [4].

Study of the influence of the composition of manganese ores from different deposits on the quality of silicomanganese. From the production data of the enterprise, 2500 kg of manganese raw materials, 810 kg of metallurgical coke, 340 kg of quartzite, and 500 kg of sinter are consumed according to approved standards for one ton of the finished product of the MnS 17 grade (according to state standard 4756-91) and 80 kg of coal concentrate. Based on this, for laboratory tests to smelt 150 g of alloy, the same components were used in the following ratio: 375 g of manganese raw materials, 121.5 g of metallurgical coke, 51 g of quartzite, 74 g of manganese agglomerate and 12 g of coal concentrate. However, with different quality of raw materials, the amount of one or another component can change for the necessary chemical reactions to occur. We compiled two charge mixtures (Table 3).

**Table 3.** Composition of the charge mixture in the smelting of silicomanganese using ores from different deposits (research)

| Raw material component | Alloy No. 1, g<br>Zhezdy ore | Alloy No. 2, g<br>Akzhar-Sarytum ore |
|---|---|---|
| Manganese ore | 375 | 346 |
| Quartzite | 51 | 51 |
| Coal coke | 113,2 | 113,2 |
| Coal concentrate | 14,6 | 13,5 |
| Iron filings | 3,75 | 4,5 |
| Manganese agglomerate | 81,4 | 74 |

Based on Table 3 and subsequent analysis of the research data obtained, we consider it possible to recommend the following compositions of the charge mixture for production conditions (Table 4, Fig.1).

**Table 4.** Composition of the charge mixture in the smelting of silicomanganese using ores from different deposits (research)

| Raw material component | Alloy No. 1, g<br>Zhezdy ore | Alloy No. 2, g<br>Akzhar-Sarytum ore |
|---|---|---|
| Manganese ore | 2500 | 2307 |
| Quartzite | 340 | 340 |
| Coal coke | 755 | 755 |
| Coal concentrate | 97 | 90 |
| Iron filings | 25 | 30 |
| Manganese agglomerate | 550 | 500 |

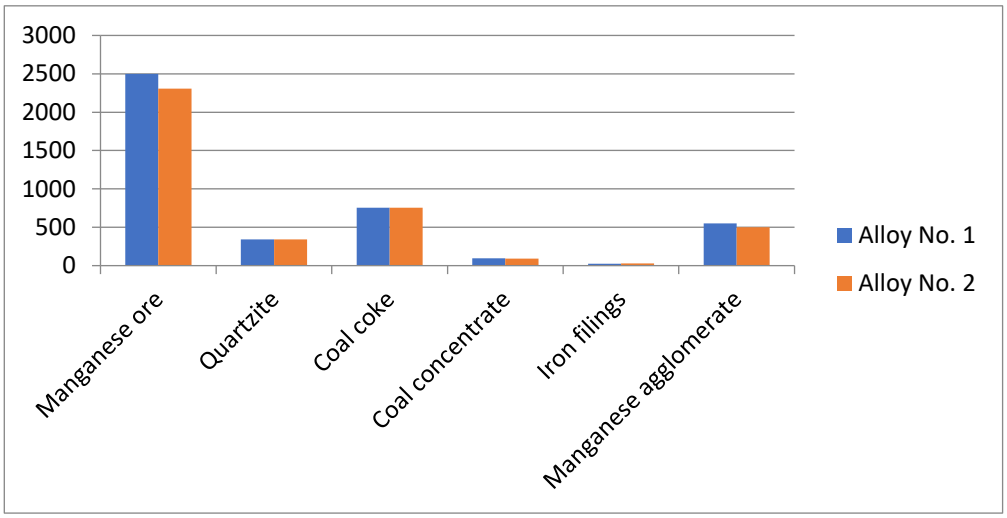


**Fig. 1.** – Composition of the charge mixture when smelting silicomanganese using ores from different deposits

## 2. Results and discussion

When comparing two alloys obtained in laboratory conditions, silicomanganese using Zhezdy manganese ore (Figure 2) showed the following:

- uneven particle size or the presence of large lumps;
- grey or black color (usually high-quality silicomanganese has a lighter color), which indicates a low-quality product.

Part of the separated alloy is necessary for chemical analysis. Quantitative and qualitative analysis was carried out by two methods: express analysis using a spectrometer, and chemical analysis for the manganese content in the alloy was used to confirm the accuracy of the results.

When conducting chemical analyses of this alloy (Table 5), a high content of impurities such as iron, sulfur and phosphorus is noted. This will affect the working properties of the alloy and the quality of steel alloying in further production.

**Table 5.** Chemical composition of silicomanganese using Zhezdy ore, %

| Mn | Si | C | P | S |
|---|---|---|---|---|
| 57,2 | 23,6 | 3,7 | 0,7 | 0,02 |

Silicomanganese, obtained using ore from the Akzhar-Sarytuma deposit (Figure 3.19) as manganese raw material, is lighter in appearance than the previous one, granular material with a metallic luster. Its chemical composition (Table 6) is similar to the composition of silicomanganese according to state standard 4756-91 grade MnS17, smelted at the enterprise.

**Table 6.** Chemical composition of silicomanganese using Akzhar-Sarytum ore

| Mn | Si | C | P | S |
|---|---|---|---|---|
| 65,4 | 16,7 | 2,5 | 0,3 | 0,02 |

Based on the results of the studies, it is clear that the quality of the alloy decreases when using manganese ore with a low content of the main component. The lower quality of the alloy also leads to a lower price when exporting products but at a lower cost. However, under current conditions, the selection of the necessary raw materials is becoming more complicated. Thus, we can talk about the use of "poor" manganese ores of the Zhezdy deposit only taking into account the possible improvement of existing raw materials by adding ore from "rich" deposits, for example, the Chiatura deposit (Georgia) with a total Mn content of 42%. This ore is currently used at Asia FerroAlloys LLP.

Studying the influence of the composition of manganese ores on the quality of silicomanganese is an important task for optimizing the process of its production and increasing production efficiency. Research has shown that the quality of silicomanganese depends on many parameters: the content of manganese, silicon, phosphorus and sulfur, as well as grain size and degree of oxidation. Also, as practice shows, ores with a high silicon content and low manganese content can lead to the formation of "plugs" in furnaces, which complicates the firing process and can reduce the quality of the product [5].

In addition, the influence of phosphorus and sulfur content on the quality of silicomanganese is also significant, since they can introduce undesirable impurities into the product. Therefore, it is necessary to conduct careful chemical analysis of manganese ores before using them for the production of silicomanganese. Thus, studying the influence of the composition of manganese ores on the quality of silicomanganese is important for optimizing the production process and increasing production efficiency. This leads to improved product quality and reduced production costs.

**Conclusion**

Studying the influence of the composition of manganese ores on the quality of silicomanganese is an important issue for optimizing the production process and increasing production efficiency. Silico-manganese is produced by mixing the ore with coke and silicon, then firing the mixture in a high-temperature furnace to extract the necessary elements from the raw materials. In addition, phosphorus and sulfur content also have a significant impact on the quality of silicomanganese as they create undesirable impurities in the product. Therefore, before using manganese ore in the production of silicomanganese, a thorough chemical analysis and determination of the parameters of the influence of one or another component of the ore material on the quality of the resulting ferroalloy is necessary. To determine the factors influencing the quality of silicomanganese, the chemical composition of manganese ores from the Zhezdy and Akzhar-Sarytum deposits was studied. As a result, it was determined that the quality of the resulting ferroalloys depends on:

- from the content of manganese, silicon and harmful impurities (phosphorus and sulfur);
- on grain size;
- on the degree of oxidation.

Having studied the influence of the chemical composition of manganese ores on the quality of ferroalloys, it should be noted that when using manganese ore from the Zhezdy deposit with total manganese of 16.6%, the resulting quality and grade do not meet the requirements of the state standard.

Research results have shown that the quality of the alloy decreases when using manganese ores with a low content of main components. The low quality of the alloy also makes it cheaper to export, but this reduces the cost of the alloy. However, the current situation makes it difficult to select the necessary raw materials, so it is possible to improve the existing Kazakhstani raw materials by adding ore from rich deposits.

**References**

[1] Nefedov P.Ya. On the quality requirements of carbon reducing agents for ore electrothermia processes – Coke and Chemistry No. 8, 2018, P. 24-32.

[2] A.C. No. 565942 (USSR). Charges for smelting silica manganese. I.P.Rogachev, I.P.Kazachkov, A.G.Kucher, etc. Published in B.I., No. 27, 2019.

[3] Matyushenko V.I., Khitrik S.I., Dekhanov N.M. et al. Mastering the smelting of silicomanganese in ferroalloy furnaces RPZ-48 Ferrous Metallurgy, Byull. sci.-tech. inform. No. 2 (670), 1972, P. 30-33.

[4] Zhuchkov V.I., Smirnov L.A., Zaiko V.T., Voronov Yu.I. Technology of manganese ferroalloys. Part 1. High–carbon ferromanganese – Yekaterinburg: Ural Branch of the Russian Academy of Sciences, 2017. - 381 p.

[5] Yessengaliyev D., Baisanov S., Issagulov A., Zayakin O. et al. Thermodynamic diagram analysis (TDA) of MnO-CaO-$Al_2O_3$-$SiO_2$ and phase compositions of slag in refined ferromanganese production // Croatia Croatian Metalurgical Society Metalurgija, Vol. 3 (58), 2019, P. 291-294.

**Information of the authors**

**Naboko Elena Petrovna,** candidate of technical sciences, Abylkas Saginov Karaganda Technical University
e-mail: lena_nep@mail.ru

**Issagulova Diana Aristotelevna,** doctor of PhD, Abylkas Saginov Karaganda Technical University
e-mail: isagulovada@mail.ru

**Platonova Elena Sergeevna,** master of technical sciences, Abylkas Saginov Karaganda Technical University
e-mail: danilina1969@list.ru

**Yudakova Valeriya Alexandrovna,** master of technical sciences, Abylkas Saginov Karaganda Technical University
e-mail: lera-mlp@mail.ru

**Pitirimova Tatyana Vladimirovna,** master of philology, Abylkas Saginov Karaganda Technical University
e-mail: 26061984@mail.ru

**DOI 10.52209/2706-977X_2023_4_27 IRSTI 55.36.31 UDC 669.184:669.141.245**

# Experience in Repairing Converter Gas Boiler-Coolers

**Ivashin Yu.A., Lyssenko I.P., Starkov V.A.***
LLP "Praktika-T", Temirtau, Kazakhstan
*corresponding author

**Abstract.** In this project technical solutions were made based on many year working experience with boiler equipment in the converter shop. This project will reduce converter downtime and increase the volume of the produced liquid metal up to 400 thousand tenge and, taking into account all the extraneous factors, It will increase the economic effect of the ArcelorMittal Temirtau JSC by about $180 million per year without investing additional funds. This will also lead to increasing jobs in the Karaganda region and the opportunity to compete with foreign suppliers. In addition, when working at this project, the share of Kazakhstan content in the manufactured products of the ArcelorMittal Temirtau JSC increases. The use of the repair method described in the article will lead to improving the environmental situation in the city of Temirtau, since the normal functioning of the converter gas boiler-cooler directly affects the pollution of emitted impurities into the city atmosphere. Germany and Russia are interested in this technology.

**Keywords:** welding seam, lining, converter, lack of penetration.

## Introduction

At the first glance, metallurgy seems to be an extremely conservative industry, where changes and modernization are not the trend of today but something that comes after a long run-in and experimentation [1]. But this is not so. The growing demand for high-quality steel grades will require special attention to equipment, both at new and modernized enterprises, and digitalization will be an integral part of all the stages of production activity [2, 3].

For example, such complex equipment as converter gas boiler-coolers is an extremely important thing in production [4]. They are designed to cool and to recover heat from waste gases of steelmaking converters, and serve to generate steam for technological needs [5]. The design of boiler-coolers takes into account high thermal loads, their cyclicity, and high dust content of gases leaving the neck of the converters [6]. Therefore, it is extremely important to carry out their timely and high-quality repairs.

There are several types of boiler-coolers for converter gases mounted behind converters with upper oxygen purge [7]. Such boilers are used for afterburning converter gases and cooling combustion products to the temperature of 250-300 °C, at which it becomes possible to clean them from dust [8].

Cooling converter gases by admission of cold air is associated with high energy costs to remove the gas-air mixture and the loss of a significant amount of heat. To reduce the temperature of gases from the 100-130 ton converter without burning CO, the required amount of air for dilution is 25 $m^3/s$ [9]. When gas is uniformly mixed with air, the CO concentration in the mixture is 7.15%, which is much lower than the lower limit mixture for CO (12.5%). However, it is almost impossible to avoid explosive local concentrations, so CO has to be burned off. In this case, the air flow rate is about 140 $m^3/s$, the power of the electric motors of the smoke exhausters behind the gas cleaning to remove the gas-air mixture reaches 5000 kW [10].

The temperature and pressure at which the elements and devices of the boiler-cooler operate, provide increased requirements for quality and reliability during their production and repair. In addition, the production of boiler equipment is not serial. In some ways it is unique, and this is where the additional complexity of manufacturing and repairing industrial boilers lies.

## 1. Research methods

The technology of repairing boiler-coolers leads to increasing the overhaul period by paralleling repair work, as well as better and more efficient repairs in the presence of a reserve recoiling part of the boiler-cooler and repairing the heating surfaces of the boiler stationary part in a large-block way on special repair stands, which in turn reduces repair time and increases the service life of equipment.

With proper operation of boiler-coolers, repairs to the recoiling part can be carried out once every 12-14 months. This is extremely important to take it into account, since when the converters are heavily loaded, the enterprise does not have the opportunity to frequently stop production to carry out routine repairs.

The proposed technology makes it possible to combine the work of overhauling the recoil part and the lining of the converter. This period of downtime can be used to repair and to replace the recoiling and stationary parts of the boiler-coolers. If there is a reserve recoiling part, the replacement can be carried out within 7-9 days.

**2. Results and discussion**

From 2014 to 2020, the team of authors participated in mounting and repair work in the converter shop of the metallurgical plant of the ArcelorMittal Temirtau JSC. The company performed such work as repair of recoiling parts of converter gas boiler-coolers, replacement of skirts and heating surfaces of the stationary part of boiler-coolers.

Within this period, in the territory of the production workshop of the Praktika-T company, there were manufactured hinges, skirts, heating surfaces of the stationary part, filling caissons and the recoiling part of the boiler-coolers (Figure 1).

a)

b)

c)

a) skirt; b) filling caissons; c) recoiling part

**Fig. 1.** – Manufacturing the parts of boiler-coolers at the the Praktika-T company

To manufacture the recoiling part of the boiler-cooler, a special assembly stand and platforms for transportation were used. In 2018, the work was completed to mount and to put into operation the ecoiling part of the boiler-cooler of converter No. 1.

Boiler-coolers for converter gases are designed to cool and to recover heat from the waste gases of steelmaking converters (Figure 2). They also serve to generate steam for the technological needs of the plant. The design of boiler-coolers takes into account high thermal loads, their cyclicity, and a high dust content of gases leaving the neck of the converters.

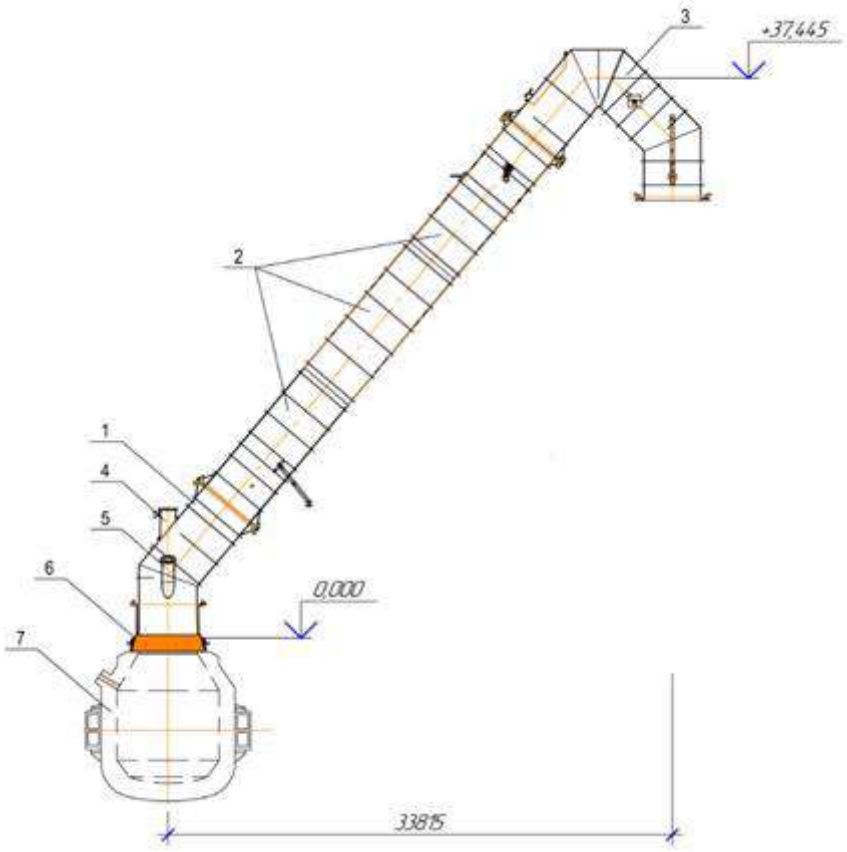


1 – recoiling part; 2 – stationary inclined part; 3 – stationary bypass elbow; 4 – tuyere caisson; 5 – caisson of bulk materials; 6 – skirt; 7 – converter

**Fig. 2.** – Converter gas boiler-cooler

This design of boiler-coolers is particularly complicated for carrying out repair work at the boiler work site. One of the difficulties is the forced use of operational welds to weld the heating surfaces of the boiler-cooler. During the repair work at the working sites of boiler-coolers, there were encountered such difficulties as inaccessibility of welding work, which entailed the need to perform operational welds.

The operational welding seam is used in a hard-to-reach place, through a technical window. It is mainly used in pipe welding. This type of welding seam has two significant disadvantages: frequent lack of penetration and the ingress of foreign particles in the form of slag and scale from welding into the pipe. This is extremely unacceptable for the normal functioning of the boiler-cooler. This significantly reduces the quality of the repair work performed, since the performance and service life of the boiler directly depends on the purity of the water.

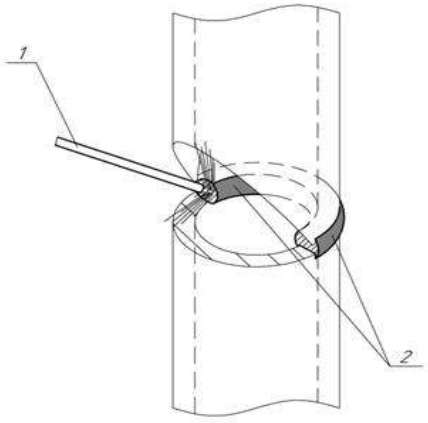


1 – welding seam; 2 – welding the pipe from the inside

**Fig. 3.** – Operational welding seam

Based on the experience gained, there was proposed changing the technology of repairing boiler-coolers.

The repair technology developed includes the presence of a reserve recoiling part of the boiler-cooler and the repair of heating surfaces of the stationary part of the boiler using a large-block method on special repair stands.

With proper operation of boiler-coolers, repairs to the recoiling part can be carried out once every 12-14 months. Due to a high load on converters, it is not possible to frequently stop production for routine repairs.

Once a year, the work on converter lining is carried out. The developed technology makes it possible to combine the work on the overhaul of the recoiling part and the lining of the converter. This period of downtime can be used to repair and to replace the recoiling and stationary parts of the boiler-coolers. If there is a reserve recoiling part, the replacement can be carried out within 7-9 days. The failed recoiling part is placed on a special repair stand, which will allow performing a complete troubleshooting and high-quality repair, preparing it for further re-use until the next repair of the recoiling part in operation. Repairing the recoiling part on a special repair stand gives full access to welding work, the ability to test and to perform repair technology at a high level that is difficult to do when repairing the working platforms of a boiler-cooler.

The blocks for repairing heating surfaces of the stationary part of the boiler-cooler are assembled at the repair site using special repair stands. Replacing the damaged part with one large block makes it possible to carry out repair work quickly and efficiently. The blocks for repair can also be assembled at the manufacturer's factory.

**Conclusions**

The main advantages of the proposed technology of repairing boiler-coolers is significant increasing the quality of repair work, which in turn halves the costs and the time of its implementation. It is worth noting that this repair technology will be effective if the metal smelting technology is strictly followed, since adherence to the technology directly affects the service life of the power equipment of the converter shop.

This will also lead to increasing jobs in the territory of the converter shop and the opportunity to compete with a foreign supplier.

In addition, when working at this project, the share of Kazakhstan content in the manufactured products of the ArcelorMittal Temirtau JSC increases.

**References**

[1] Ghorbani Y., Nwaila G., Zhang S, Hay M. Repurposing legacy metallurgical data part II: Case studies of plant performance optimization and process simulation // Minerals Engineering, Volume 160, 2021, 106667

[2] Branca, T.A., Fornai, B., Colla, V., Murri M.M., Streppa E., Schroder A.J. The Challenge of Digitalization in the Steel Sector //Metals 2020, 10, P. 288

[3] Colla, Valentina & Pietrosanti, Costanzo & Malfa, Enrico & Peters, Klaus. Environment 4.0: How digitalization and machine learning can improve the environmental footprint of the steel production processes //Matériaux & Techniques, 2021, P.108

[4] Clews R.J. Chapter 10 - Natural Gas and LNG Project Finance for the International Petroleum Industry, 2016, P. 169-185

[5] Hussam Jouhara, Navid Khordehgah, Sulaiman Almahmoud, Bertrand Delpech, Amisha Chauhan, Savvas A. Tassou Waste heat recovery technologies and applications //Thermal Science and Engineering Progress, Volume 6, June 2018, P. 268-289

[6] Zuo Z., Dong X., Luo S., Yu Q. Waste Heat Recovery from Converter Gas by a Filled Bulb Regenerator: Heat Transfer Characteristics. Processes 2023, 11, P. 915

[7] Hendrik Le Roux, W.B. Drummond Reducing/eliminating gas emissions from pierce smith converters //The South African Institute of Mining and Metallurgy The Third Southern African Conference on Base Metals, 2020, P. 71 - 86

[8] Akash Singh, Vivek Sharma, Siddhant Mittal, Gopesh Pandey, Deepa Mudgal, Pallav Gupta An overview of problems and solutions for components subjected to freside of boilers //International Journal of Industrial Chemistry, 2018, 9, P. 1–15

[9] Mi, Jiaxing & Wang, Feifei & Li, Pu Bo & Dally, Bassam Modified Vitiation in a Moderate or Intense Low-Oxygen Dilution (MILD) Combustion Furnace //Energy & Fuels, 2011, P. 26.

[10] Dryden I.G.C. The Efficient Use of Energy (Second Edition), Butterworth-Heinemann, Chapter 10 - Boiler plant and auxiliaries, 1982, 200 – 248.

**Information of the authors**

**Ivashin Yuri Alexeyevich**, technical supervisor, LLP "Praktika-T"
e-mail: ivashin.ya@mail.ru

**Lyssenko Irina Petrovna,** leading design engineer, LLP "Praktika-T"
e-mail: l_irina_p@mail.ru

**StarkovVladislav Aleksandrovich**, leading design engineer, LLP "Praktika-T"
e-mail: vadian_95@mail.ru

**DOI 10.52209/2706-977X_2023_4_32 IRSTI 55.43.03 UDC 629.113.012**

# Free and Forced Vibrations of the Carrier Beam of the Vehicle Chassis

**Akhmediev S.K., Filippova T.S., Oryntayeva G.Zh.,**
**Tazhenova G.D., Mikhailov V.F.***
Abylkas Saginov Karaganda Technical University, Karaganda, Kazakhstan
*corresponding author

**Abstract.** The article is dealing with the stress-strain state of the carrier beam of the two-axle vehicle chassis for a dynamic perturbing load that occurs in the process of driving along the unevenness of the road, taking into account the elastic characteristics of the spring suspension. When analyzing the ride smoothness, it is necessary to take into account low-frequency forced vibrations caused by road irregularities, as well as free low-frequency vibrations. The dynamic calculation was carried out by the force method. In this case, the expansion of a given arbitrary dynamic load is performed in terms of the main modes of vibration. The calculation for free and forced vibrations was made by an exact analytical method, taking into account the elastic pliability of the axial supports of the beam. In the course of the study, the external dynamic forces acting on the structure under consideration, reduced to three-point masses, were determined and three forms of free vibrations were obtained. The results of the study can be used to optimize the design of the truck chassis and to improve their reliability and safety in operation. By understanding the behavior of a suspension system under dynamic loads, engineers can design stronger, more reliable designs that can withstand the stress of transporting heavy loads over rough roads. In general, this study contributes to the development of more efficient and safer transport systems.

**Keywords:** Free and forced vibrations; Chassis; Carrier beam; Stress-strain state; Amplitude.

## Introduction

Any complex multi-mass mechanical systems, including vehicles interact with the external environment. This system includes sprung masses such as a body, a driver, passengers, a cargo and unsprung masses of axles. The masses interact with each other through the elastic and dissipative elements of the suspension, tires and seats that allow their moving relative to each other.

There are a lot of mathematical models that are used to study the dynamics of a vehicle. Works [1]–[4] present a complete analysis of various models from the designer's point of view, for example, changing the suspension stiffness, the damping coefficient, optimizing the form of its elements using the modal finite element analysis [5]. In [6], a nonlinear model of a dynamic system was considered using the Simscape environment in the MATLAB/Simulink. The results show a significant reduction in the amount of displacement and acceleration of the sprung mass during rebound and roll compared to the linear model, therefore, the non-linear spring elements work well in most static and dynamic conditions.

When analyzing ride smoothness, it is necessary to take into account low-frequency forced vibrations caused by road irregularities, as well as free low-frequency vibrations. For trucks, it is sufficient to take into account vibrations of the body and suspension, in which vertical vibrations of the masses and angular vibrations of the body in the longitudinal and transverse vertical planes of the vehicle are analyzed. The quality of the suspension depends directly on the amplitude-frequency characteristics of the kinematic and vibration effects [7], [8]. In [9] it was found that increasing nonlinear stiffness leads to changing the magnitude of oscillation amplitudes and frequencies that affect the overall stability of the vehicle. In [10], forced vibrations of a four-axle vehicle with a double spring suspension were studied. For its mathematical model a numerical solution was obtained for the critical value of external excitation, within which vibration becomes stable. In this case, the suspension parameters were selected from the required amplitude value.

The vehicle movement occurs in conditions of uneven roads, which leads to vibrations of the body, seats and is accompanied by vibration loads on the human body and the vehicle mechanisms. In [11], the influence of road roughness, vehicle speed, suspension stiffness and damping on vehicle characteristics was studied. In addition, inverse problems were solved, such as determining the reaction of the road surface when the vehicle was moving [12].

One of the ways to reduce vibration loads is to regulate the damping of oscillations of the sprung masses of the vehicle suspension system. In works [13], [14], the dynamics of the vehicle suspension behavior when it moves along the unevenness of the roadway, as well as through the forest area, is studied. The results show that the proposed suspension can provide a significant reduction in vibration levels, and the appropriate selection of the material leads to decreasing the deflection and resulting stresses, improving dynamic performance and increasing the service life.

The developers of a new technology pay great attention to the development of new suspension elements in the form of inerter [15] and hydraulic integrated suspension [16].

**1. Methods and solutions**

When designing vehicles of various designs and carrying capacity, it is necessary to calculate the load-bearing structures of the vehicle chassis, taking into account their movement along the unevenness of the road, i.e., to calculate them under kinematic disturbances.

Forced vibrations of chassis structures are caused by kinematic perturbation of the spring suspension of a moving vehicle.

The object of study is the carrier beam of the vehicle chassis with constant bending stiffness with resiliently pliable supports (A, B) (Figure 1) that work in bending from the dynamic impact caused by the kinematic movement of the spring suspension.

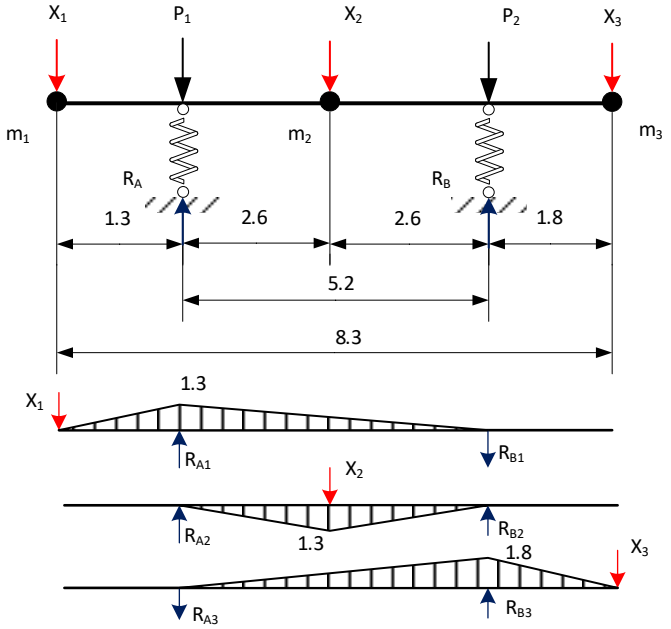


**Fig. 1.** - The carrier beam of the two-axle vehicle chassis

Dynamic calculations of the above construction will be carried out by the force method. Direct dynamic calculation of the structure under study is carried out in the following algorithmic sequence:

1. In order to simplify the calculation, there is first performed the expansion of the given arbitrary dynamic load in terms of the main vibration modes.

2. There is performed the calculation for free vibrations (in the absence of a disturbing force) as a system with three degrees of freedom in order to determine the frequency spectrum and modes of natural vibrations with studying the dependence of frequency characteristics on the changes in the degree of pliability (cushioning) of the chassis supports.

3. There is performed the calculation for forced vibrations from the disturbing harmonic load that occurs when vehicles move along uneven roadways with studying the changes in the amplitudes of dynamic movements from the degree of pliability of the chassis wheel bearings.

**2. Calculation for free vibrations**

Let's calculate the coefficients of the pliability matrix (Figure 1). Vereshchagin's method, representative by graph multiplication method, shows the effective ability to determine displacement resulting from deformation body of bending structures. The advantages of this method are the integrating process derived from Maxwell-Mohr:

$$\begin{aligned}
\delta_{11} &= \int_0^l \frac{(M_1^2)}{EJ_x}dx + \frac{\sum_{i=1,2}(R_{1,i}^2)}{C_i} = 2.375 \cdot 10^{-3}\ kN \cdot m \\
\delta_{22} &= \int_0^l \frac{(M_2^2)}{EJ_x}dx + \frac{\sum_{i=1,2}(R_{2,i}^2)}{C_i} = 1.2054 \cdot 10^{-3} kN \cdot m \\
\delta_{33} &= \int_0^l \frac{(M_3^2)}{EJ_x}dx + \frac{\sum_{i=1,2}(R_{3,i}^2)}{C_i} = 3.402 \cdot 10^{-3} kN \cdot m \\
\delta_{12} &= \delta_{21} = \int_0^l \frac{(M_1)(M_2)}{EJ_x}dx + \sum_{i=1,2}\frac{(R_{1,i} \cdot R_{2,i})}{C_i} == -0.144 \cdot 10^{-3}\ kN \cdot m
\end{aligned} \quad (1)$$

$$\delta_{13} = \delta_{31} = \int_0^l \frac{(M_1)(M_3)}{EJ_x} dx + \sum_{i=1,2} \frac{(R_{1,i} \cdot R_{3,i})}{C_i} == -0.0098 \cdot 10^{-3}\ kN \cdot m$$

$$\delta_{32} = \delta_{23} = \int_0^l \frac{(M_2)(M_3)}{EJ_x} dx + \sum_{i=1,2} \frac{(R_{2,i} \cdot R_{3,i})}{C_i} == -0.365 \cdot 10^{-3}\ kN \cdot m$$

where $\delta_{ii}$ is the coefficient of the pliability matrix, $M_i$ is the bending moment, $C_i$ is the coefficient of stiffness, $E$ is the elastic modulus, $J_x$ is the moment of inertia, $R_{i,i}$ is the support reaction.

Let's make a secular equation ($\tau = 0.25 \cdot 10^4\ kg$, $C = 1{,}15 \cdot 10^4\ \frac{kN}{m}$):

$$D = m \begin{vmatrix} \delta_{11} - \lambda & \delta_{12} & \delta_{13} \\ \delta_{21} & \delta_{22} - \lambda & \delta_{23} \\ \delta_{31} & \delta_{32} & \delta_{33} - \lambda \end{vmatrix} = 0 \qquad (2)$$

where $D$ is the matrix determinant, $\lambda_i$ is the root of the secular equation, $m$ is the mass.

$$\lambda_i = \frac{1}{\omega_i^2 m} \qquad \omega_i = \sqrt{\frac{1}{\lambda_i m}} \qquad (3)$$

where $\omega_i$ is the circular frequence.

Solution (2) gives the following values:

$$\lambda_1 = 8{,}653 \cdot 10^{-4} \frac{s^2}{kg} \quad \omega_3 = 59{,}52\ s^{-1}$$

$$\lambda_2 = 5{,}979 \cdot 10^{-4} \frac{s^2}{kg} \quad \omega_2 = 40{,}90\ s^{-1}$$

$$\lambda_3 = 2{,}823 \cdot 10^{-4} \frac{s^2}{kg} \quad \omega_1 = 34\ s^{-1}$$

Based on the intrinsic vectors $\bar{v}_{ik}$ ($i = 1, 2, 3;\quad k = 1, 2, 3$) there is built the forms of intrinsic vibrations in the form of the "standing" waves (Figure 2).

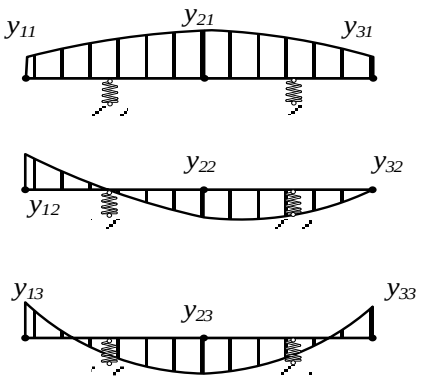


**Fig. 2.** - Beam intrinsic vibrations forms

**II Calculation for forced vibrations**

Let's consider the case of uniform motion of a vehicle along the road with the speed $v$ [17]–[19].

In this case, the abscissa of motion is $x = vt$ and the path profile has the equation $x = \Delta(vt)$. Then the perturbing inertia force is taken in the form of a harmonic load

$$P_i(t) = P_{0,i} \sin \theta t \quad (i = 1, 2) \qquad (4)$$

where $P_i(t)$ is the perturbing force, $P_{0,i}$ is the amplitude perturbing force.

$$\theta = \pi v / l_0 \tag{5}$$

where $\theta$ is the disturbing force frequency, $v$ is the velocity of movement, $l_0$ is the average length.
The amplitude perturbing force is

$$P_{0,i} = m_i f_{0,i} \left(\frac{\pi^2 v^2}{l_0^2}\right) = m_i f_{0,i}(\theta^2). \tag{6}$$

where $f_{0,i}$ is the kinematic excitation parameter.

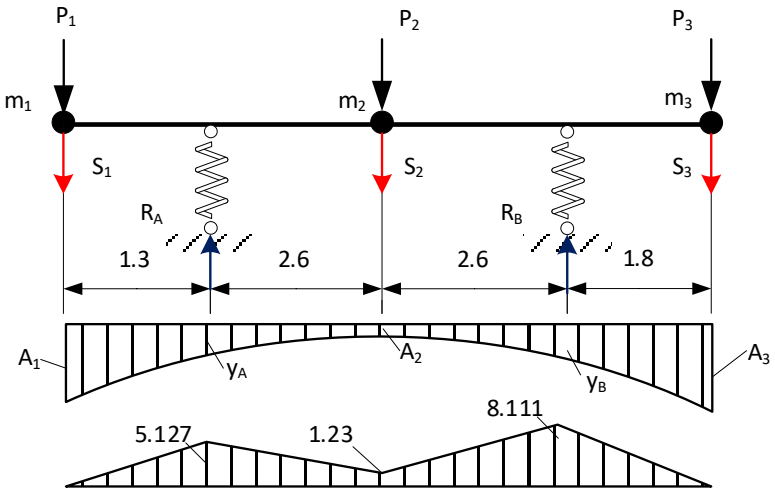


**Fig. 3.** - Forced vibration scheme

Let's consider the steady-state oscillations of the system (in the absence of movement resistance forces). The parameters of forced vibrations are as follows:

a) at an arbitrary moment

- $y_i(t) = A_i \sin \theta t$ is the displacement, $A_i$ is the displacement amplitude;
- $J_i(t) = -m_i \ddot{z}_i = \theta^2 m_i A_i \sin \theta t$ is the inertia force;
- $P_i(t) = P_{0i} \sin \theta t$ is the perturbing force;
- $S_i(t) = (P_{0i} + \theta^2 m_i A_i) \sin \theta t$ is the external dynamic force;

b) in the amplitude state

- $A_i$;
- $J_i = \theta^2 m_i A_i$;
- $P_{0i}$;
- $S_i = P_{0i} + J_i = P_{0i} + \theta^2 m_i A_i$.

For the further calculations there is accepted the following:
$v = 16.67 \ \frac{m}{s}$; $l_0 = \frac{l}{4} = 2.075 \ m$; ($l = 8.3 \ m$, Figure 1).

Based on formula (5):

$$\theta = \frac{3{,}14 \cdot 16{,}67}{2{,}075} = 25{,}23 \ s^{-1}.$$

The pliability matrix of the system (with $n = 3$):

$$[\delta] = \begin{bmatrix} \delta_{11} & \delta_{12} & \delta_{13} \\ \delta_{21} & \delta_{22} & \delta_{23} \\ \delta_{31} & \delta_{32} & \delta_{33} \end{bmatrix} \tag{7}$$

Having accepted $C_1 = 1{,}15 \cdot 10^4 \ \frac{kN}{m}$, there is obtained:

$$[\delta] = 10^{-3} \begin{bmatrix} 2.375 & -0.144 & -0.0098 \\ -0.144 & 1.205 & -0.365 \\ -0.0098 & -0.365 & 3.402 \end{bmatrix}$$

The deflection vector, taking into account (7):

$$\vec{\mathrm{A}} = \begin{bmatrix} \mathrm{A}_1 \\ \mathrm{A}_2 \\ \mathrm{A}_3 \end{bmatrix} = [\delta]\vec{S} = \\ = 10^{-3} \begin{bmatrix} 2.375 & -0.144 & -0.0098 \\ -0.144 & 1.205 & -0.365 \\ -0.0098 & -0.365 & 3.402 \end{bmatrix} \cdot \begin{bmatrix} S_1 \\ S_2 \\ S_3 \end{bmatrix} \tag{8}$$

$$\vec{\Delta}_{i,P_0} = \begin{bmatrix} \Delta_{1P_0} \\ \Delta_{2P_0} \\ \Delta_{3P_0} \end{bmatrix} = [\delta]\vec{P}_{0,i} = \\ = 10^{-3} \begin{bmatrix} 2.375 & -0.144 & -0.0098 \\ -0.144 & 1.205 & -0.365 \\ -0.0098 & -0.365 & 3.402 \end{bmatrix} \cdot \begin{bmatrix} P_{01} \\ P_{02} \\ P_{03} \end{bmatrix} \tag{9}$$

By (6) we obtained:

$$P_{0,i} = m_i f_{0,i}(\theta^2) = 0{,}25 f_{0,i}(25{,}23)^2 = 159{,}14 f_{0,i}$$

The amplitude equations [20]:

$$\begin{cases} \left[\delta_{11}m_1 - \left(\frac{1}{\theta^2}\right)\right] A_1 + \delta_{12}m_2 A_2 + \delta_{13}m_3 A_3 = -\frac{\Delta_{1P_0}}{\theta^2} \\ \delta_{21}m_1 A_1 + \left[\delta_{22}m_2 - \left(\frac{1}{\theta^2}\right)\right] A_2 + \delta_{23}m_3 A_3 = -\frac{\Delta_{2P_0}}{\theta^2} \\ \delta_{31}m_1 A_1 + \delta_{32}m_2 A_2 + \left[\delta_{33}m_3 - \left(\frac{1}{\theta^2}\right)\right] A_3 = -\frac{\Delta_{3P_0}}{\theta^2} \end{cases} \tag{10}$$

The equations for amplitudes of external dynamic forces:

$$\begin{cases} \left[\delta_{11} - \left(\frac{1}{m_1\theta^2}\right)\right] S_1 + \delta_{12}S_2 + \delta_{13}S_3 = -\frac{P_{01}}{m_1\theta^2} \\ \delta_{21}S_1 + \left[\delta_{22} - \left(\frac{1}{m_2\theta^2}\right)\right] S_2 + \delta_{23}S_3 = -\frac{P_{02}}{m_2\theta^2} \\ \delta_{31}S_1 + \delta_{32}S_2 + \left[\delta_{33} - \left(\frac{1}{m_3\theta^2}\right)\right] S_3 = -\frac{P_{03}}{m_3\theta^2} \end{cases} \tag{11}$$

Here

$$m_1 = m_2 = m_3 = 0{,}25 \cdot 10^4 \ kg; \ \theta = 25{,}23 \ s^{-1}.$$

Let's open equation (9) taking into account the initial data (with $\theta/\omega_1 = 0{,}742$):

$$\begin{cases} -3.909S_1 - 0.144S_2 - 0.0098S_3 = -15.899 \sin 25.23t \\ -0.144S_1 - 5.079S_2 - 0.365S_3 = -17.72 \sin 25.23t \\ -0.0098S_1 - 0.365S_2 - 2.882S_3 = -14.139 \sin 25.23t \end{cases} \tag{12}$$

Having solved system (12), there is obtained:

$$S_1 = 3.944 \cdot 10^4 N, S_2 = 3.053 \cdot 10^4 N, S_3 = 4.506 \cdot 10^4 N.$$

Figure 3 shows the diagram of bending moments under external dynamic forces. Based on (8), there is determined

$$\mathrm{A}_1 = 8.765 \cdot 10^{-3} \ m, \ \mathrm{A}_2 = 1.917 \cdot 10^{-3} \ m, \ \mathrm{A}_3 = 14.176 \cdot 10^{-3} \ m.$$

Based on the beam deflection curve (Figure 3) there is expressed the beam deflections dependence through the interpolation polynomial [21] with ($\mathrm{n} = 2$ is the degree of the polynomial, $\mathrm{a}_0 = \mathrm{A}_1$):

$$y(x) = a_0 + a_1 x_i + a_2 x_i^2 = 10^{-3}(8.765 + a_1 x_i + a_2 x_i^2) \tag{13}$$

According (13) (Figure 3) there is written down the system of algebraic equations for determining the values of $\mathrm{a}_1$, $\mathrm{a}_2$, ($\mathrm{x}_1 = 3.9m$, $\mathrm{x}_2 = 8.3m$):

$$\left.\begin{array}{l} 8.765 \cdot 10^{-3} + 3.9a_1 + 15.21a_2 = 1.917 \cdot 10^{-3} \\ 8.765 \cdot 10^{-3} + 8.3a_1 + 68.89a_2 = 14.176 \cdot 10^{-3} \end{array}\right\} \quad (14)$$

Solving system (14), there is determined:

$$a_1 = -3.89 \cdot 10^{-3}; \quad a_2 = 0.547 \cdot 10^{-3} \quad (15)$$

Substitute expressions (15) into equation (13):

$$y(x_i) = (8.765 - 3.89x_i + 0.547x_i^2) \cdot 10^{-3} \quad (16)$$

where $y(x_i)$ is the ordinate of displacement and the interpolation polynomial of 2nd degree obtained (16).
Based on (16) there is calculated:

- $x_i = 1.3\ m$ (on the A support): $y_A = 4.6337 \cdot 10^{-3}\ m$;
- $x_i = 6.5\ m$ (on the B support): $y_B = 6.597 \cdot 10^{-3}\ m$.

The accuracy of calculating the intermediate deflections of a beam can be increased by taking into account the interpolation polynomial of a higher degree, i.e., taking $n > 2$.

Next, there will be studied the effect of the elastic pliability of supports *A* and *B* on the dynamic forces $P_1$, $P_2$ of the beam in Figure 1. Let's take the values of the pliability coefficients of supports *A*, *B* in the range $(0 \ldots 0.87 \cdot 10^{-4}\ \frac{m}{kN})$ (the results are in Table 1).

According to Table 1, there are constructed graphs of the circular frequencies of free vibrations dependence on the pliability coefficients of supports *A* and *B* (indicated by $k_i$ ).

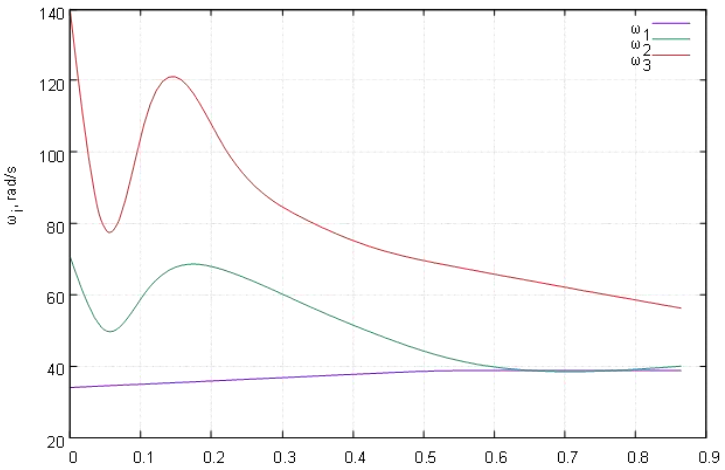


**Fig. 4.** - The $\omega_i = f(k_i)$ $(k_i \cdot 10^{-4}\frac{m}{kN})$ dependences

Let's write the expressions of interpolation polynomials according to Table 1 for the analytical determination of the circular frequencies of free vibrations $\omega_i$ $(i = 1,\ 2,\ 3)$ and the amplitudes of dynamic displacements $y_i$ $(i = 1,\ 2,\ 3)$ depending on changing the $C_i$ and $k_i$values.

**Table 1.** Dynamic parameters for the beam depending on the coefficients of stiffness $C_i$ and pliability $(k_i = 1/C_i)$ of the *A* and *B* supports

| $C_i \cdot 10^4, \frac{kN}{m}$ | $k_i \cdot 10^{-4}, \frac{m}{kN}$ | Circular frequencies $\omega_i, s^{-1}$ | | | Dynamic movement amplitudes, m | | |
|---|---|---|---|---|---|---|---|
| | | $\omega_1$ | $\omega_2$ | $\omega_3$ | $A_1 \cdot 10^{-3}$ | $A_2 \cdot 10^{-3}$ | $A_3 \cdot 10^{-3}$ |
| 1.15 | 0.87 | 34.0 | 40.90 | 59.52 | 8.765 | 1.917 | 14.176 |
| 2.3 | 0.434 | 36.67 | 49.24 | 74.16 | 5.286 | -0.894 | 9.5723 |
| 10 | 0.1 | 38.74 | 64.42 | 109.69 | 3.6988 | -2.00 | 6.072 |
| 20 | 0.05 | 35.83 | 51.57 | 83.28 | 7.005 | 0.595 | 11.054 |
| 30 | 0.033 | 35.95 | 48.27 | 75.95 | 7.565 | 1.01 | 12.04 |
| ∞ | 0.0 | 38.48 | 70.48 | 135.96 | 2.561 | 7.89 | 5.36 |

According to Table 1, it can be seen that with increasing the pliability of supports *A*, *B* (Figure 3), the circular frequencies of natural vibrations of the beam first increase monotonically, and then decrease monotonically, while the values reach the minimum $\omega_i$ $(i = 1,\ 2,\ 3)$ at the value of $k_i \approx 0{,}21 \cdot 10^{-4}\ \frac{m}{kN}$.

The dependences of circular frequencies (by analogy with (16)) are as follows:

$$\left.\begin{array}{l}\omega_1 = 34.0 + 40.63k_i - 79.182k_i^2 \\ \omega_2 = 40.90 + 238.53k_i - 503.16k_i^2 \\ \omega_3 = 59.52 + 532.49k_i - 1144.86k_i^2\end{array}\right\}. \quad (17)$$

The first derivatives from the frequencies:

$$\begin{array}{l}\omega_1' = 40.63 - 79.182k_i = 0;\ k_i^1 = 0.513 \cdot 10^{-4}\ \frac{m}{kN}, \\ \omega_2' = 238.53 - 503.16k_i = 0;\ k_i^2 = 0.474 \cdot 10^{-4}\ \frac{m}{kN}, \\ \omega_3' = 532.49 - 1144.86k_i = 0;\ k_i^3 = 0.465 \cdot 10^{-4}\ \frac{m}{kN}.\end{array} \quad (18)$$

Now let's study the dynamic movement amplitudes $\mathrm{A}_i$ depending on the changing of pliability coefficients $k_i$.

We accept the next values $C_2 = 2.3 \cdot 10^4\ \frac{kN}{m}$, $\theta = 25.23\ s^{-1}$, $\tau = 0.25 \cdot 10^4\ kg$. According to (7) and (11) we obtain:

$$[\delta] = 10^{-3}\begin{bmatrix} 1.6685 & -0.3608 & 0.2619 \\ -0.3608 & 0.9883 & -0.5826 \\ 0.2619 & -0.5826 & 2.6955 \end{bmatrix}$$

$$\begin{cases} -4.6155S_1 - 0.3608S_2 + 0.2619S_3 = -15.899 \\ -0.3608S_1 - 5.296S_2 - 0.5826S_3 = -17.72 \\ 0.2619S_1 - 0.5826S_2 - 3.5885S_3 = -14.139 \end{cases}$$

Having solved system, there is determined:

$$S_1 = 3.457\ \cdot 10^4 N;\ \ S_2 = 2.582\ \cdot 10^4 N;\ S_3 = 3.7734\ \cdot 10^4 N.$$

$\mathrm{A}_1 = 5.286 \cdot 10^{-3}\ m,\ \mathrm{A}_2 = -0.8939 \cdot 10^{-3}\ m,\ \mathrm{A}_3 = 9.5723 \cdot 10^{-3}\ m$ .

For $C_3 = 10 \cdot 10^4\ kN/m$, $\theta = 25.23\ s^{-1}$, $\tau = 0.25 \cdot 10^3 kg\ s^2/m$:

$$[\delta] = 10^{-3}\begin{bmatrix} 1.125 & -0.5282 & 0.4711 \\ -0.5282 & 0.8209 & -0.75 \\ 0.4711 & -0.75 & 2.005 \end{bmatrix}$$

$$\begin{cases} -5.159S_1 - 0.5282S_2 + 0.4711S_3 = -15.899 \\ -0.5282S_1 - 5.4631S_2 - 0.75S_3 = -17.72 \\ 0.4711S_1 - 0.75S_2 - 4.279S_3 = -14.139 \end{cases}$$

There is obtained:

$$S_1 = 3.1187\ \cdot 10^4\ N;\ S_2 = 2.502\ \cdot 10^4\ N;\ \ S_3 = 3.2092\ \cdot 10^4\ N.$$

$$\mathrm{A}_1 = 3.6988 \cdot 10^{-3}\ m,\ \mathrm{A}_2 = -2.0 \cdot 10^{-3}\ m, \qquad \mathrm{A}_3 = 6.0272 \cdot 10^{-3}\ m$$

Let's write down interpolation polynomials (11) for dynamic movement amplitudes $\mathrm{A}_i$ (based on the data of Table 1):

a) for $\mathrm{A}_1$:

$\mathrm{A}_1 = a_0 + a_1 x_i + a_2 x_i^2;\ \mathrm{a}_0 = 8.765$

$$\begin{cases} \Delta \mathrm{x}_1 = 0.87 - 0.434 = 0.436 \\ \Delta \mathrm{x}_2 = 0.1 - 0.434 = 0.334 \end{cases}$$

$5.286 = 8.765 + \mathrm{a}_1(0.436) + \mathrm{a}_2(0.436)^2$

$3.6988 = 8.765 + \mathrm{a}_1(0.334) + \mathrm{a}_2(0.334)^2$

$$\begin{cases} 0.436\mathrm{a}_1 + 0.190\mathrm{a}_2 = -3.479; \\ 0.334\mathrm{a}_1 + 0.11156\mathrm{a}_2 = -5.0662 \end{cases}$$

$$\begin{cases} a_1 = -38.723 \\ a_2 = 70.55 \end{cases}$$
$$A_1 = 10^{-3}(8.765 - 38.723k_i + 70.55k_i^2) \quad (19)$$

b) for $A_2$:

$$A_2 = a_0 + a_1x_i + a_2x_i^2;\ a_0 = 1.917$$
$$-0{,}894 = 1.917 + a_1(0.436) + a_2(0.436)^2$$
$$-2.00 = 1.917 + a_1(0.334) + a_2(0.334)^2$$
$$\begin{cases} 0.436a_1 + 0.190a_2 = -2.811 \\ 0.334a_1 + 0.11156a_2 = -3.917 \end{cases}$$
$$\begin{cases} a_1 = -29.03 \\ a_2 = 51.825 \end{cases}$$
$$A_2 = 10^{-3}(1.917 - 29.03k_i + 51.82k_i^2) \quad (20)$$

c) for $A_3$:

$$A_3 = a_0 + a_1x_i + a_2x_i^2;\ a_0 = 14{,}176$$
$$9.5723 = 14.176 + a_1(0.436) + a_2(0.436)^2$$
$$6.072 = 14.176 + a_1(0.334) + a_2(0.334)^2$$
$$\begin{cases} 0.436a_1 + 0.190a_2 = -4.6037 \\ 0.334a_1 + 0.11156a_2 = -8.104 \end{cases}$$
$$\begin{cases} a_1 = -69.173 \\ a_2 = 134.505 \end{cases}$$
$$A_3 = 10^{-3}(14.176 - 69.173k_i + 134.505k_i^2) \quad (21)$$

According to equations (19-21), Table 1 is supplemented (with $k_i = 0.05$; $k_i = 0.033$).
Figure 5, according to Table 1, shows the dependence of the amplitudes of the dynamic displacements $A_i$ $(i = 1,\ 2,\ 3)$ of the beam (Figure 3) depending on the pliability coefficients of the supports ($A$, $B$) (on the values $k_i$).

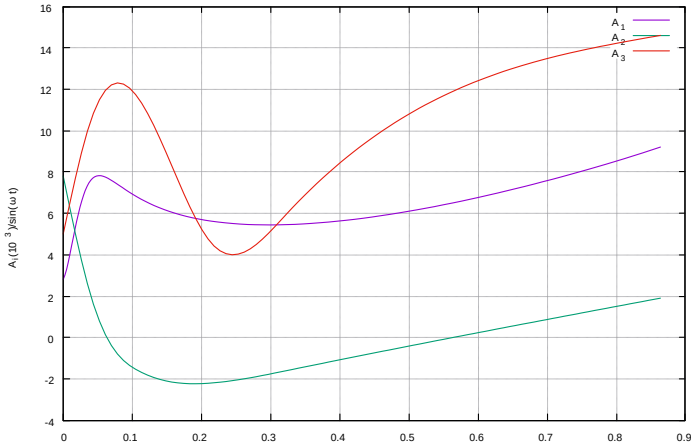


**Fig. 5.** - The $A_i = f(k_i)$ $(k_i \cdot 10^{-4}\ \frac{m}{kN})$ dependences

**Conclusions**

In this work, there is studied the stress-strain state (SSS) of a carrier beam for the two-axle truck chassis for the dynamic perturbing load that occurs during the movement of the vehicle (the calculation for kinematic excitation $x = \Delta(t)$) along the road irregularities, taking into account the elastic characteristics of the spring suspension.

In the process of studies, the external dynamic forces acting on the structure under consideration were determined, reduced to three-point masses. The dependencies $\omega_i = f(k_i)$ , $A_i = f(k_i)$ were given.

For the accepted coefficient of compliance of supports $A$ and $B$ (the $k = 0.87 \cdot 10^{-4}\ \frac{m}{kN}$ value) there were determined:

- the forms of free vibrations at frequencies $\omega_1,\ \omega_2,\ \omega_3$;
- the diagram of amplitudes of dynamic changes;
- the diagram of amplitudes of dynamic bending moments.

According to the results of the study, it was established: all three forms of free vibrations are complex, they have one, two or three "standing" waves with alternating plus and minus signs with zero displacements at the locations of the corresponding masses $\tau_1,\ \tau_2,\ \tau_3$.

Here there is observed the effect of the elastic pliability of the supports A, B.

When changing the value of the pliability coefficient $k_i$ (Table 1), the following is observed:

- the main tone $\omega_1$ is almost independent of the value $k_i$ (Figure 4);
- the first ($\omega_2$) and second ($\omega_3$) overtones change along a complex trajectory: they either sharply decrease, or sharply increase (at $k_i = 0,0 \dots 0.324 \cdot 10^{-4}\ m/kN$), then stabilize (monotonically decreasing at $k_i > 0.216 \cdot 10^{-4}\ m/kN$);
- in Figure 5, the nature of changing the amplitudes of dynamic mass displacements $A_i$ ($i = 1,\ 2,\ 3$) is also quite complex: the amplitude of the second mass ($A_2$) (in the span of the beam) changes monotonously, while the amplitudes of the first ($A_1$) and third ($A_3$) masses (on the beam consoles) have a complex-changing character with a sharp increase and decrease within the $k_i = 0,0 \dots 0.216 \cdot 10^{-4}\ m/kN$ limits and a monotonous change in values at $k_i > 0.216 \cdot 10^{-4}\ m/kN$.

The proposed theoretical developments and applied results can be used in scientific research in the field of mechanics of a solid deformable body, as well as in the process of designing load-bearing structures of various types in mechanical engineering, construction and vehicles, i.e. when solving specific problems of strength, rigidity and stability that arise in the process of design and construction.

**References**

[1] S. Talukdar, A. Mazumdar, M. Mullasseril, K. Kalita, and A. Ujjwal,"Mathematical modeling in vehicle ride dynamics," SAE Technical Papers, 2012, doi: 10.4271/2012-01-0056.

[2] W. Wang, X. Cao, and S. Cheng, "Structural failure analysis of a sport utility vehicle chassis," ACM International Conference Proceeding Series, pp. 100–103, May 2018, doi: 10.1145/3230876.3230886.

[3] W. Wang, Z. Hou, Z. Zhou, and S. Cheng, "Stress Relaxation of a Sport Utility Vehicle Chassis Using a Dynamic Force Counteracting Approach," MATEC Web of Conferences, vol. 249, Dec. 2018, doi: 10.1051/MATECCONF/201824903001.

[4] J. N. Wang, T. Ye, W. Sun, and Q. N. Wang, "Vibration isolation performance of energy-regenerative semi-active suspension with variable stiffness and damping," Jilin Daxue Xuebao (Gongxueban)/Journal of Jilin University (Engineering and Technology Edition), vol. 47, no. 3, pp. 701–708, May 2017, doi: 10.13229/J.CNKI.JDXBGXB201703002.

[5] N. Karsakova et al., "Calculation of the boring bar design for static rigidity and strength with simultaneous boring of a stepped hole with further optimization" Journal of Applied Engineering Science, pp. 1–13, Jan. 2023, doi: 10.5937/jaes0-40340.

[6] D. Nigwal, D. K. Pasi, and M. Chouksey, "Effect of nonlinear conical springs on the vibration characteristics of seven degree-of-freedom car model using MATLAB/Simscape," International Journal of Dynamics and Control, 2022, doi: 10.1007/S40435-022-01007-2.

[7] K. Saeedi, R. J. Alkhoury, R. B. Bhat, and A. K. W. Ahmed, "Ride dynamic analysis of a hybrid discrete and continuous vehicle model," SAE Technical Papers, 2008, doi: 10.4271/2008-01-2671.

[8] S. Dharani Kumar, S. Sendhil Kumar, and K. Arun Kumar, "Investigation of forced frequency in a commercial vehicle suspension system," Mechanics and Mechanical Engineering, vol. 22, no. 4, pp. 967–974, 2018, doi: 10.2478/mme-2018-0076.

[9] J. Yao, J. Q. Zhang, M. M. Zhao, and Z. J. Wei, "Analysis of dynamic stability of nonlinear suspension," Advances in Mechanical Engineering, vol. 10, no. 3, Mar. 2018, doi: 10.1177/1687814018766648.

[10] S. K. Kargapol'tsev, V. E. Gozbenko, B. O. Kuznetsov, Y. I. Karlina, and A. I. Karlina, "The effect of the periodic driving force on a system with two degrees of freedom," Journal of Physics: Conference Series, vol. 1333, no. 5, p. 052009, Oct. 2019, doi: 10.1088/1742-6596/1333/5/052009.

[11] L. Zuo and P. S. Zhang, "Energy harvesting, ride comfort, and road handling of regenerative vehicle suspensions," Journal of Vibration and Acoustics, Transactions of the ASME, vol. 135, no. 1, 2013, doi: 10.1115/1.4007562.

[12] R. X. Xia, J. H. Li, J. He, and D. F. Shi, "Effect analysis of vehicle system parameters on dynamic response of pavement," Mathematical Problems in Engineering, vol. 2015, 2015, doi: 10.1155/2015/561478.

[13] A. E. Nabawy, A. M. M. Abdelhaleem, S. S. Alieldin, and A. A. Abdelrahman, "Study of the dynamic behavior of porous functionally graded suspension structural systems using finite elements methods," Steel and Composite Structures, vol. 35, no. 5, pp. 697–713, Dec. 2022, doi: 10.12989/SCS.2022.45.5.697.

[14] A. Pazooki, D. Cao, S. Rakheja, and P. E. Boileau, "Experimental and analytical evaluations of a torsio-elastic suspension for off-road vehicles," SAE Technical Papers, pp. 326–338, 2010, doi: 10.4271/2010-01-0643.

[15] C. A. Morales, "Complete results for free and forced vibrations of inerter-added one-degree-of-freedom systems," Journal of Vibroengineering, vol. 21, no. 6, pp. 1564–1573, Sep. 2019, doi: 10.21595/JVE.2019.20554.

[16] W. Smith and N. Zhang, "Experimental and theoretical investigation into the dynamics of a half-car with an interconnected passive suspension," SAE Technical Papers, 2009, doi: 10.4271/2009-01-0579.

[17] A. F. Smirnov, A. V. Alexandrov, B. Ya. Lashchenikov, and N. N. Shaposhnikov, Construction mechanics. Dynamics and stability of structures. Moscow: Stroyizdat, 1984.

[18] F. Cheli and G. Diana, Advanced Dynamics of Mechanical Systems. Cham: Springer International Publishing, 2015. doi: 10.1007/978-3-319-18200-1.

[19] K. A. Seeler, System Dynamics. New York, NY: Springer New York, 2014. doi: 10.1007/978-1-4614-9152-1.

[20] T. Filippova and S. Akhmediev, Theoretical foundations of dynamics and stability of mechanical systems. Germany: LAP LAMBERT Academic Publishing, 2016.

[21] M. Schäfer, "Computational engineering - Introduction to numerical methods," Computational Engineering - Introduction to Numerical Methods, pp. 1–321, 2006

**Information of the authors**

**Akhmediev Serik Kabultaevich**, candidate of technical sciences, Abylkas Saginov Karaganda Technical University
e-mail: s.ahmediev@kstu.kz

**Filippova Tatyana Silinyevna**, candidate of technical sciences, Abylkas Saginov Karaganda Technical University
e-mail: tsxfilippova@mail.ru

**Oryntayeva Gulzhaukhar Zhunuskhanovna**, senior lecturer, Abylkas Saginov Karaganda Technical University
e-mail: oryntaeva70@mail.ru

**Tazhenova Gulzada Dauletkhanovna**, candidate of technical sciences, Abylkas Saginov Karaganda Technical University
e-mail: gulzada_2604@mail.ru

**Mikhailov Valentin Feliksovich**, candidate of technical sciences, Abylkas Saginov Karaganda Technical University
e-mail: v.mihaylov@kstu.kz

**DOI 10.52209/2706-977X_2023_4_42 IRSTI 67.09.55 UDC 625.72**

# Study of Pavement Anomalies Using GPR of OKO-2 series

**Iskakov K.[1], Sagindykov K.[1], Mukhambetkaliyev K.[2]*, Kalmenov K.[3], Seitkhanova A.[3]**
[1]L.N. Gumilyov Eurasian National University, Astana, Kazakhstan
[2]Kazakhstan Center for Modernization and Development of Housing and Communal Services, Astana, Kazakhstan
[3]RSE on REU «National Center for the Quality of Road Assets», Astana, Kazakhstan
*corresponding author

**Abstract**. This paper reflects the main aspects of the methodology for studying road pavement structures using non-invasive research methods. The technology for diagnosing highways using OKO-2 georadar complexes has been studied. Non-invasive methods are based on the principle of radar with the generation of electromagnetic high-frequency wave pulses through pavement structures. The scientific work was carried out within the framework of grant funding for a scientific and technical project on the topic: AP19680361 - "Development of computing technologies for diagnosing road pavement of highways." Based on the analysis of radargrams and instrumental examination of highway anomalies using mathematical methods, it is planned to determine numerical algorithms using the theory of ill-posed problems, mathematical apparatus: equations of mathematical physics, optimization methods and the theory of difference schemes. This work is of scientific and practical interest for improving the methodology for georadar inspection of highways.

**Key words.** Mechatronics of georadar research, Ground penetrating radar, OKO-2 device, road pavement, diagnostics, anomaly, algorithm, transport and operational state, interpretation of radargrams, images of road pavement structures, radar principle

Introduction. Timely diagnosis of road pavement structure is the main stage in the inspection of highways. RSE on the PCV "National Center for the Quality of Road Assets" in its activities on road asset management carries out diagnostics and instrumental examination of many thousands of kilometers of roads.

The methodology for diagnosing highways using Oko-2 georadar equipment is described in [1-8]. Analysis of georadargrams allows for high-quality diagnostics and visual assessment of the condition of roads during operation, without opening the structural layers of the road pavement. The result of non-invasive diagnostics is the identification of abnormal sections of roads that do not meet regulatory requirements for their transport and operational condition. Based on georadar data and the results of a highway survey, the types and composition of the main works and activities for maintenance, repair and reconstruction are determined in order to improve their transport and operational condition to the required level.

Research methods. The operation of the OKO-2 georadar is based on the principle of radar - electromagnetic high-frequency wave pulses passing through road pavement structures from several centimeters to several meters, depending on the parameters of the antenna unit, make it possible to create detailed images of road pavement structures displaying anomalies. By road pavement anomalies we mean surface defects in the form of holes, potholes, cracks, subsidence, cavities and voids formed during operation.

Table 1 shows the main technical characteristics of the antenna units of the OKO-2 georadar complexes with antenna units (AB-400R, AB-1000R).

**Table 1.** General technical characteristics of OKO-2 antenna units

| Antenna unit AB-400R | Antenna unit АБ-1000P |
|---|---|
| Work with a gap of up to 30 cm<br>Center frequency 400 MHz<br>Sounding depth 3 m | Work with a separation of 30 cm<br>Center frequency 1000 MHz<br>Maximum probing depth up to 1.5 m |

The principle of operation is based on the phenomenon of reflection of electromagnetic waves from surfaces on which electrical properties change. The main parameter of the medium is its dielectric constant (□). During GPR sounding, the GPR moves along the surface being surveyed or with a slight separation (depending on the type of antenna unit). An electromagnetic wave in soil (or other research medium) is reflected from the boundaries of layers that have excellent dielectric properties. The GPR consists of a transmitting (source) and receiving (receiver) antenna. The source emits an electromagnetic wave of a given frequency, and at each point of the distance a trace is recorded - the dependence of the signal amplitude on the time of arrival of the reflection. A set of traces along the entire distance makes up a radargram. The first reflection on the radargram is called a direct wave (forward signal). The direct wave is in most cases the same for all profile traces (Figure 1). It is determined by the design of the antenna and the surface of the profile. Other waves on the radargram are waves reflected from any boundaries of layers or local objects in the soil (or other research environment).

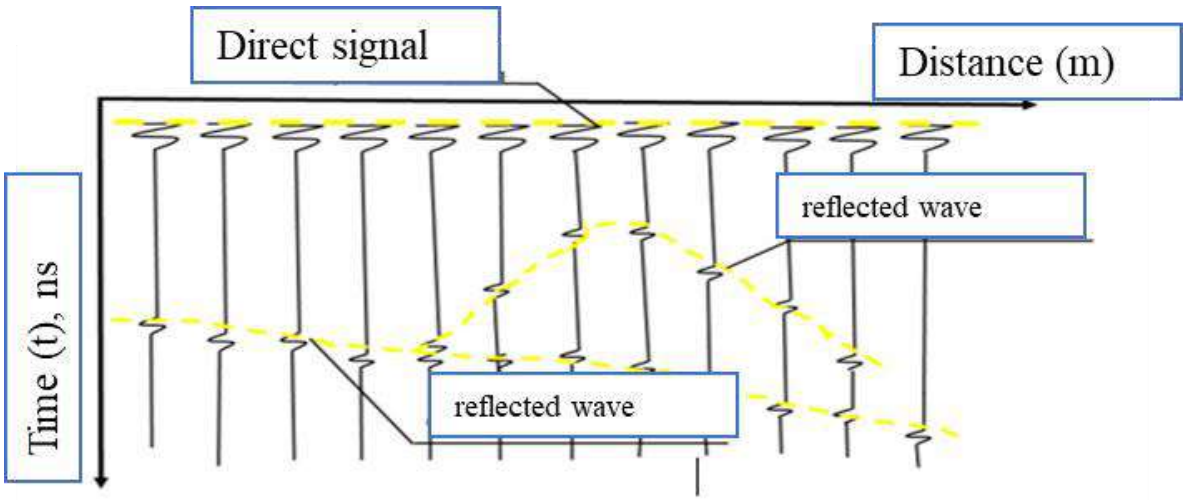


**Fig. 1.** - Schematic representation of the principle of the ground penetrating radar method

Reflected signals from local objects on the radargram are displayed in the form of a characteristic hyperbola (Figure 2). The object from which the reflected wave originated is located at the point corresponding to the vertex of the hyperbola. Application of the georadar method to highlight the boundaries of soil layers, detect local objects, etc. perhaps due to differences in electrical properties. The main properties are electrical resistivity ρ and dielectric constant ε.

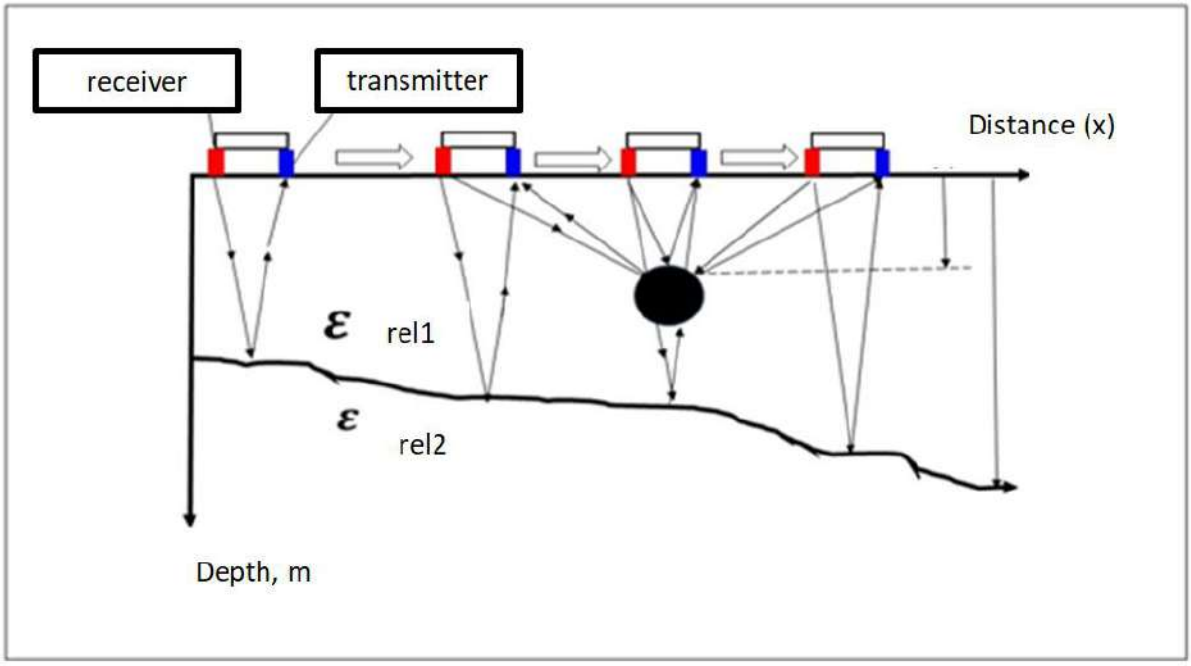


**Fig. 2.** - The principle of the formation of reflected waves from the boundary of two media and a local object

Specific electrical resistance determines the attenuation of the electromagnetic field in the medium, and, consequently, the depth of the study. The lower the attenuation, the greater the depth the field will penetrate, that is, we will receive a response from rocks at greater depths. Almost all substances, except pure metal, can be classified as dielectrics with finite conductivity. In this regard, the concept of relative dielectric constant of a substance was introduced.


**Fig.3.** - Mobile road diagnostic laboratory with installed Oko-2 ground penetrating radars, with AB-400R and AB-1000R antenna units

Scientific results. The software supplied with the device uses an engineering method for interpreting radargrams, which consists of comparing the obtained radargrams with a database of known species. Experimentally established or physically based formulas for determining the geoelectric section are also used.

Preparatory work for the Oko-2 georadar for inspecting automotive work includes: 1. installation of the antenna unit using a universal suspension on the vehicle; 2. mounting the displacement sensor on the rear wheel of the car; 3. selection of antenna unit and sounding parameters.

The georadar series: "Oko-2", with the antenna unit AB-400R and AB-1000R, is intended for diagnostics of road surfaces (highway routes). This modification allows you to take real data at a travel speed of 60-80 km/h. The device determines the thickness of the layers of the road surface, during repeated research it determines changes in the boundaries of the layers, and issues recommendations to conduct additional research in the zone of decompaction of the road pavement.

Interpretation of georadar data - obtaining the most complete information about the structure of road pavement, expressed in the form of geological sections: determining changes in the thickness of the layers of road pavement; determination of the soil moisture zone; determining the spatial outline of the bottom of the layers; determination of groundwater infiltration paths; identification of defects made during road works; release of foreign inclusions in the soil.

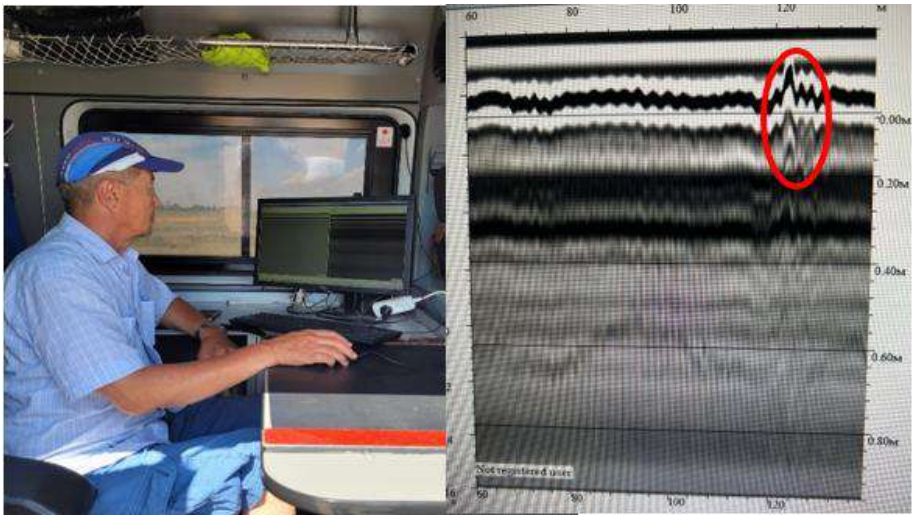

**Fig. 4.** - Radargram with an anomaly of pavement defects

A georadar survey of the subgrade, base and road surfaces was carried out using the Oko-2 series device (AB-400R and AB-1000R) with the following results:

section of the road being repaired under the project “Major repairs of the road “Eastern Bypass of Astana - Art. Saryoba", km 0-23 and km 23-41.

During the departure, a georadar measurement was carried out using the Oko-2 device (AB-400R and AB-1000R) on the laid structural layers of road pavement:

- the bottom layer of the base is made of crushed stone-peved mixture C4;
- the top layer of the base is made of crushed stone-sand mixture C6, treated with Portland cement M-400 in an amount of 7%.
- the bottom layer of coating with hot coarse-grained porous asphalt concrete Grade 2.

Similarly, a section of the R-2 "Astana – Korgalzhyn" highway, km 49-51, was examined.

**Fig 4.** - Surveying with ground penetrating radar anomalies and defects in the road surface of the R-2 "Astana – Korgalzhyn" highway, km 49-51

Georadar measurements using the Oko-2 device (AB-400R and AB-1000R) on the section of the R-2 Astana-Korgalzhyn highway with the entrance to the Korgalzhyn Nature Reserve were carried out in places where there were obvious defects and anomalies - destruction and potholes on the surface and base of the road.

**References**

[1] Vladov M. L., Starovoitov A. V. Introduction to georadar. – M., 2005. – 153 p.
[2] Lai W.L., Kou S.C., Tsang W.F., Poon C.S. Characterization of concrete properties from dielectric properties using ground penetrating radar // Cement and Concrete Research, Vol. 39, Issue 8, 2009, P.687 - 695.
[3] GOST R 58349–2019 Road pavement. Methods for measuring the thickness of pavement layers.
[4] Tosti F., Patriarca C., Slob E., Benedetto A., Lambot S. Clay content evaluation in soils through GPR signal processing // Journal of Applied Geophysics, 2013, Vol. 97, P. 69 - 80.
[5] Venkateswara Rao B., Sevu M., Narasaiah V. Dielectric constants determination of overburden materials using ground penetrating radar // J. Ind. Geophys. Union, 2020, Vol. 24(5), P.64 - 74.
[6] R RK 218-176-2020 Instructions for assigning the service life between repairs of road pavements based on a georadar survey.
[7] Starovoitov A.V. Interpretation of ground penetrating radar data: Tutorial. – M.: Moscow State University Publishing House, 2008. – 192 p.
[8] Zajícová K., Chuman T. Application of ground penetrating radar methods in soil studies: A review // Geoderma. – 2019, Vol.343, P. 116 - 129.

**Information of the authors**

**Iskakov Kazizat Takuadinovich,** d.ph.-m.s., professor, L.N. Gumilyov Eurasian National University
e-mail: kazizat@mail.ru

**Sagindykov Kakim Moldabekovich,** c.t.s., associate professor, L.N. Gumilyov Eurasian National University
e-mail: ksagin@mail.ru

**Mukhambetkaliyev Kairat Kuanskalievich,** c.t.s., general manager, JSC "Kazakhstan Center for Modernization and Development of Housing and Communal Services"
e-mail: k.mukhambetkaliyev@zhkh.kz

**Kalmenov Kanat Baydullaevich,** magister's student, leading expert, RSE on REU "National Center for the Quality of Road Assets"
e-mail: k.kalmenov1@sapaortalygy.kz

**Seitkhanova Anel Valikhanovna,** magister's student, head of department, RSE on REU "National Center for the Quality of Road Assets"
e-mail: a.seitkhanova@sapaortalygy.kz